The Influence of Idealized Heterogeneity on Wet and Dry Planetary Boundary Layers Coupled to the Land Surface

EDWARD G. PATTON, PETER P. SULLIVAN, AND CHIN-HOH MOENG

National Center for Atmospheric Research, Boulder, Colorado*

(Manuscript received 29 August 2003, in final form 16 November 2004)

ABSTRACT

This manuscript describes numerical experiments investigating the influence of 2–30-km striplike heterogeneity on wet and dry convective boundary layers coupled to the land surface. The striplike heterogeneity is shown to dramatically alter the structure of the convective boundary layer by inducing significant organized circulations that modify turbulent statistics. The impact, strength, and extent of the organized motions depend critically on the scale of the heterogeneity λ relative to the boundary layer height z_i. The coupling with the land surface modifies the surface fluxes and hence the circulations resulting in some differences compared to previous studies using fixed surface forcing. Because of the coupling, surface fluxes in the middle of the patches are small compared to the patch edges. At large heterogeneity scales ($\lambda/z_i \sim 18$) horizontal surface-flux gradients within each patch are strong enough to counter the surface-flux gradients between wet and dry patches allowing the formation of small cells within the patch coexisting with the large-scale patch-induced circulations. The strongest patch-induced motions occur in cases with $4 < \lambda/z_i < 9$ because of strong horizontal pressure gradients across the wet and dry patches. Total boundary layer turbulence kinetic energy increases significantly for surface heterogeneity at scales between $\lambda/z_i = 4$ and 9; however, entrainment rates for all cases are largely unaffected by the striplike heterogeneity.

Velocity and scalar fields respond differently to variations of heterogeneity scale. The patch-induced motions have little influence on total vertical scalar flux, but the relative contribution to the flux from organized motions compared to background turbulence varies with heterogeneity scale. Patch-induced motions are shown to dramatically impact point measurements in a free-convective boundary layer. The magnitude and sign of this impact depends on the location of the measurement within the region of heterogeneity.

1. Introduction

Land–atmosphere coupling is widely recognized as a crucial component of regional-, continental-, and global-scale numerical models. Predictions from these large-scale models are sensitive to small-scale surface layer processes like heat and moisture fluxes at the air–soil–vegetation interface as well as boundary layer treatments (e.g., Garratt 1993). The soil moisture boundary condition has considerable influence on medium- to long-range weather forecasts and on simulated monthly mean climatic states (e.g., Rowntree and Bolton 1983). Heterogeneous soil moisture conditions can occur on many scales both naturally (Mahrt et al. 2001) and through human modification (Weaver and Avissar 2001), and both types of heterogeneity can introduce dramatic variability in boundary layer surface forcing.

There have been a number of prior investigations into the effects of heterogeneous surface forcing on the planetary boundary layer (PBL) using high-resolution large eddy simulation (LES) (e.g., Hechtel et al. 1990; Hadfield et al. 1991; Shen and Leclerc 1995; Avissar and Schmidt 1998; Albertson and Parlange 1999; Albertson et al. 2001; Raasch and Harbusch 2001; Esau and Lyons 2002; Kustas and Albertson 2003; Letzel and Raasch 2003). Hechtel et al. (1990) used measurements to drive a relatively coarse resolution LES and found no significant modifications to homogeneous cases, which they attributed to the mean wind in their simulation. Hadfield et al. (1991) studied relatively small-scale (1.5- and 4.5-km wavelength) striplike heterogeneity under free convective conditions and found that the heterogeneity-induced organized motions in the PBL. These motions increased the horizontal and vertical velocity variances near the upper/lower boundaries and in the mid PBL, respectively. Shen and Leclerc (1995) and Raasch and Harbusch (2001) found that for small-scale patchlike heterogeneity, the inten-

* The National Center for Atmospheric Research is sponsored by the National Science Foundation.

Corresponding author address: Edward G. Patton, MMM Division, NCAR, P.O. Box 3000, Boulder, CO 80307-3000.
E-mail: patton@ucar.edu

sity of the organized motions increased when the horizontal scale of the heterogeneity increased to about the PBL height. When investigating land surface forcing that is fixed in time, Avissar and Schmidt (1998) and Roy and Avissar (2000) found larger-scale heterogeneity continually intensified the organized motions when the heterogeneity increased from 2 to 40 km. As Roy and Avissar (2000) speculated, Letzel and Raasch (2003) showed that heterogeneous forcing at certain amplitudes triggers temporal oscillations in the PBL. Rather than specifying the surface fluxes (which completely decouples the forcing from the overlying atmosphere), Albertson and Parlange (1999), Albertson et al. (2001), and Kustas and Albertson (2003) investigated land surface heterogeneity using specified surface temperature and moisture. None of these studies used a dynamically coupled system where the soil responds to the atmosphere and vice versa.

Point measurements are potentially impacted by landscape-induced organized motions (Finnigan et al. 2003). To properly evaluate the surface energy balance, Mahrt (1998) suggests that the vertical flux associated with stationary eddies (which is systematically missed in current point measurement practices) must be included. Mahrt also mentions that the influence of stationary eddies diminishes when the observational level is closer to the surface. An understanding of precisely how these organized surface-induced motions affect measurements is lacking; yet such an understanding is required for proper interpretation of observations.

This paper examines the interactions between the atmosphere and the land surface using an LES model of the PBL coupled to a land surface model (LSM). Fine grids and large computational domains are used to examine the impact of a range of soil heterogeneity scales ($\lambda = 2$ to 30 km) on PBL turbulence. We use phase averaging to investigate the influence of the heterogeneity scale on the organized motions that develop. The coupling between the PBL and the land surface is found to be of fundamental importance in determining the PBL response. Resulting from the coupling, heterogeneity-induced pressure gradients and surface fluxes vary with heterogeneity scale, such that heterogeneity scales $4 \leq \lambda/z_i \leq 9$ exhibit the most intense (optimum) patch-induced motions. The contribution from these induced motions to the total vertical flux of virtual potential temperature and water vapor mixing ratio is quantified. In addition, the impact of these motions on point measurements taken at various locations within the heterogeneity is elucidated.

2. Land–atmosphere coupling

Over land surfaces during daytime hours, the surface energy balance (SEB) is thermodynamically coupled to the growth of the boundary layer through interactions between the surface sensible and latent heat fluxes, the atmospheric temperature and humidity, and the growth rate of the boundary layer by entrainment (Raupach 2000). Incoming solar radiation is partitioned by the SEB to determine the energy available to the coupled land–atmosphere system. Key variables in the SEB, such as heat and water vapor fluxes, are influenced by PBL concentrations of these quantities, which themselves are influenced by their surface fluxes, forming a negative feedback loop (McNaughton and Raupach 1996). We attempt to incorporate these important feedbacks in the study, by coupling our 3D, time-dependent LES code (Sullivan et al. 1996) to the National Centers for Environmental Prediction/Oregon State University/Air Force/Office of Hydrology (NOAH) LSM, version 2.0 (Chang et al. 1999).

The LES predicts three-dimensional and time-dependent velocity fields (u, v, w) by numerically integrating a filtered set of Navier–Stokes equations for an incompressible fluid. To incorporate buoyancy effects, the LES also integrates a thermodynamic energy equation (θ) and an equation for water vapor mixing ratio (q), which are combined to calculate virtual potential temperature ($\theta_v = \theta + 0.61\theta_q$). The effects of unresolved motions in the LES are modeled using a prognostic equation for subfilter-scale (SFS) energy (e).

In the soil, the LSM (NOAH) predicts vertical profiles of temperature (T) and moisture (Θ) by integrating a 1D set of equations for soil thermodynamic and hydrologic variables (Mahrt and Pan 1984; Pan and Mahrt 1987). The SEB couples the atmosphere and land surface and provides lower boundary conditions for the LES and upper boundary conditions for the LSM.

For nonprecipitating nonfreezing environments, the SEB for an infinitesimally thin layer at the ground surface can be written (following Brutsaert 1982; Chang et al. 1999) as $R_n = H + LE + G$, where R_n is the net radiation, H is the sensible heat flux, LE is the latent heat flux, and G is the soil heat flux. The radiation components are taken as positive toward the surface and all other components are considered positive away from the surface. See the appendix for further details.

In this coupled system, the earth's surface is an internal model layer responding to both the turbulent air above and the soil properties below; therefore this coupling provides a natural framework to investigate the influence of land surface heterogeneity on PBL structure and vice versa. It is known that under no mean wind conditions, imposed land surface heterogeneity induces organized atmospheric motions (e.g., Hadfield et al. 1991), but it has yet to be established how these organized motions feedback to dry/cool the soil, modify the surface fluxes, or modify the organized motions.

3. The LSM: Deployment, input parameters, and initial conditions

For all cases, we specify that every x, y grid point is covered by perennial grasses with a roughness length (z_0) of 0.1 m. The underlying soil contains four layers of

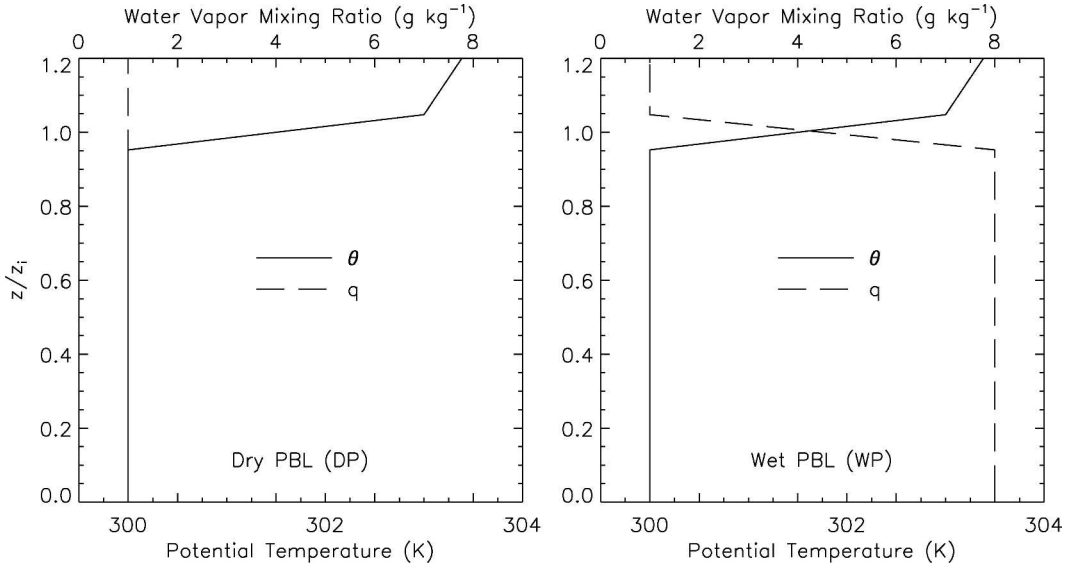

FIG. 1. Initial profiles of potential temperature (θ) and water vapor mixing ratio (q) for the dry PBL (DP) and wet PBL (WP) cases.

silty clay loam at depths 0.05, 0.20, 0.60, and 1.00 m. Since the surface is covered by grasses, we assume a constant surface albedo of 0.2 across the domain for all cases. All snow and ice components of the LSM are turned off. The exchange coefficients for momentum, heat, and moisture (C_m, C_h, C_e) across the air–soil interface are evaluated locally at every time step based on Paulson's (1970) similarity functions; C_h and C_e are assumed equal.

Initial soil conditions were taken from ground-based measurements at the Little Washita site on day 193 of the Southern Great Plains 1997 (SGP97) experiment (Jackson 1997). This day and location were chosen because nearly an inch of rain fell on the preceding 1.5 days and coincided with an intensive observing period. The observations were interpolated to the four soil levels in the LSM. To allow the LSM to equilibrate, the soil model was run offline for four complete diurnal cycles to establish initial conditions for the LES–LSM runs. Noontime conditions following these four diurnal cycles were used as the wet initial soil conditions. Dry soil conditions were obtained from noontime conditions following another seven diurnal cycles. Average initial soil conditions were obtained by picking the noontime soil conditions that provided surface fluxes nearly equal to the noontime fluxes averaged every day over the entire one-week dry-down period. The difference between volumetric surface soil moisture in the wet and dry patches is about 10%. For further details on the LSM implementation, see Patton et al. (2004).

4. Simulations

The coupled LES–LSM simulations employ (600, 100, 144) grid points in the (x, y, z) directions representing a (30, 5, 2.88)-km domain. This leads to (50, 50, 20)-m grid spacing in each of the (x, y, z) directions. Zero mean wind is imposed in both x and y, therefore the simulations are in the free convection limit. The only external forcing imposed on the system is specified through the incoming solar radiation, which is set to 700 W m^{-2} and is constant in time for all cases. We do not include an atmospheric radiation scheme, so any longwave radiation leaving the surface or scattered shortwave radiation is assumed to radiate to space.

For all of the simulations, the initial potential temperature is constant with height (300 K) below 790 m. A capping inversion is imposed (3 K/0.1 km) between 790 and 890 m, and the initial inversion height is taken as the middle of this layer, z_i = 840 m. Above 890 m the stratification is 3 K km^{-1}.

Two different PBLs are simulated with varying initial moisture content. In the first set of cases, the PBL was initialized dry (1 g kg^{-1}) throughout the entire domain [dry PBL (DP)]. The second set of cases was initialized with a relatively wet atmosphere (8 g kg^{-1}) in the PBL, dropping sharply to 1 g kg^{-1} across the initial inversion layer, between 790 and 840 m [wet PBL (WP)]. These initial moisture profiles are chosen to magnify the influence of the land surface. Figure 1 depicts the initial DP and WP atmospheric temperature and moisture conditions.

For each of the DP and WP cases, nine simulations were performed. Three of these are horizontally homogeneous with uniform soil conditions that are wet (WS), dry (DS), and average (AS), respectively. The subsequent six cases are initialized with horizontally heterogeneous soil conditions. The heterogeneity is imposed solely in the x direction as a stepfunction change be-

TABLE 1. Bulk properties for all cases. The quantities are as follows: z_i is the PBL height; λ/z_i is the ratio of the scale of the heterogeneity (λ) of the PBL height; w_* is the convective velocity; H is the surface sensible heat flux ($= \rho c_p w_* \theta_*$); LE is the surface latent heat flux ($= \rho L w_* \Theta_*$); G is the soil heat flux; $w_* \theta_{v*}$ is the total surface buoyancy flux ($= \langle w'' \theta'' \rangle + 0.61 \theta_o \langle w'' q'' \rangle$); β is the Bowen ratio (H/LE). These bulk quantities are averaged horizontally over all space and over the entire averaging period. The angle brackets denoting this averaging process are omitted for convenience. Also, n/a stands for not applicable since λ is undefined for the homogeneous cases.

Case	z_i (km)	λ/z_i	w_* (m s^{-1})	H (W m^{-2})	LE (W m^{-2})	G (W m^{-2})	$w_* \theta_{v*}$ (K m s^{-1})	β
DP-WS	1.66	n/a	2.35	259.42	138.97	80.98	0.23	1.87
DP-DS	1.85	n/a	2.69	358.74	25.32	78.22	0.32	14.17
DP-AS	1.79	n/a	2.58	326.70	59.91	81.26	0.29	5.45
DP-30S	1.71	17.55	2.52	312.02	83.04	77.16	0.27	3.73
DP-15S	1.75	8.56	2.54	312.23	83.72	77.31	0.28	3.71
DP-7.5S	1.73	4.33	2.52	310.51	83.94	78.59	0.27	3.70
DP-5S	1.72	2.91	2.51	308.05	82.97	80.90	0.27	3.71
DP-3S	1.74	1.72	2.51	307.14	82.56	80.94	0.27	3.72
DP-2S	1.74	1.15	2.51	308.05	82.86	79.83	0.27	3.72
WP-WS	1.67	n/a	2.37	264.72	133.73	80.68	0.23	1.98
WP-DS	1.79	n/a	2.67	361.68	23.77	77.20	0.32	15.22
WP-AS	1.76	n/a	2.58	329.94	56.80	81.12	0.29	5.81
WP-30S	1.70	17.61	2.52	315.22	79.73	76.92	0.28	3.95
WP-15S	1.70	8.82	2.52	316.11	80.53	75.96	0.28	3.93
WP-7.5S	1.72	4.37	2.53	315.62	80.78	76.69	0.28	3.91
WP-5S	1.72	2.91	2.52	312.61	79.76	79.71	0.28	3.92
WP-3S	1.72	1.74	2.52	311.43	78.88	80.48	0.28	3.95
WP-2S	1.73	1.55	2.52	312.05	79.02	79.73	0.28	3.95

tween wet and dry soil. We define λ as the wavelength of one complete wet and dry cycle. The wavelengths are $\lambda = 2, 3, 5, 7.5, 15, 30$ km. At initial times, the x extent of a single patch ($\lambda/2$) ranges therefore from $1.2z_i$ to $17.8z_i$. The soil conditions are homogeneous in the y direction for all simulations.

The nomenclature used in the discussion adheres to the following format: The case name includes a description of the initial PBL moisture content followed by a description of the underlying soil conditions (separated by a hyphen). For example, case DP-WS refers to the run initiated with a dry PBL and a horizontally homogeneous wet soil condition and case WP-7.5S refers to the case initialized with a wet PBL and a $\lambda = 7.5$ km wavelength heterogeneous soil condition. The rest of the names follow accordingly (see Table 1).

For normalization purposes, we define a number of parameters (z_i, w_*, θ_*, Θ_*, θ_{v*}). The PBL depth z_i is determined by finding the height in every (x, y) grid column of the largest virtual potential temperature gradient and averaging this height across all x and y. This method of locating z_i was first described as the gradient method in Sullivan et al. (1998), and further described as a wavelet method of minimum dilation in Davis et al. (2000). The convective velocity scale

$$w_* = \left\langle \frac{g}{\rho} z_i \left(\frac{H}{\theta_0 c_p} + 0.61E \right) \right\rangle^{1/3},$$

where g is the gravitational acceleration, ρ is the air density, θ_0 is a reference temperature, c_p is the specific heat of air, and E is surface water vapor mixing ratio flux; $\theta_* = \mathrm{H}/(\rho c_p w_*)$, $\Theta_* = E/(\rho w_*)$ and $\theta_{v^*} = [(H/c_p) + 0.61\theta_0 E]/(\rho w_*)$. See Table 1 for the horizontally and time-averaged values of these quantities.

5. Averaging procedures

Each simulation is initially integrated until the boundary layer averaged turbulence kinetic energy normalized by w_*^2 becomes constant, that is, quasi-stationary. This criterion was typically satisfied within 2.8–3.3 (1.9–2.5) hours for the DP (WP) cases. The time steps for the simulations were dynamically determined to satisfy the CFL criterion and ranged between 0.7 and 1.6 (1.4 and 1.7) s. Therefore, the simulations were integrated for about 6000 (4000) time steps before any statistical analysis began. Statistics are calculated over the subsequent 4000 time steps, or about 4 to 9 (8 to 10) turnover times, where a turnover time t_* is defined as z_i/w_*.

To identify organized PBL motions, we partition variables into their ensemble-averaged, phase-correlated, and background turbulence components (see Hussain and Reynolds 1970; Sullivan et al. 2000). In this method, we decompose any random signal f into

$$f(x, y, z, t) = \langle f \rangle(z) + f_p(x, z) + f'(x, y, z, t), \quad (1)$$

where $\langle f \rangle(z)$, $f_p(x, z)$, and $f'(x, y, z, t)$ are the ensemble average, phase correlated, and background turbulence variables, respectively. Here $\langle f \rangle(z)$ results from averaging over all (x, y, t) and $f_p(x, z) = \tilde{f}(x, z) - \langle f \rangle(z)$, where $\tilde{f}_p(x, z)$ is defined as an average over (y, t) and also periodically imaged in x with length λ. Thus, $f_p(x, z)$ represents the average deviation from the ensemble mean at a particular (x, z) location.[1] In presenting sta-

[1] Since the impact of the heterogeneity depends on the length scale of the heterogeneity and on the relative height compared to the PBL depth (z_i), phase-correlated results are presented in normalized variables x/λ versus z/z_i.

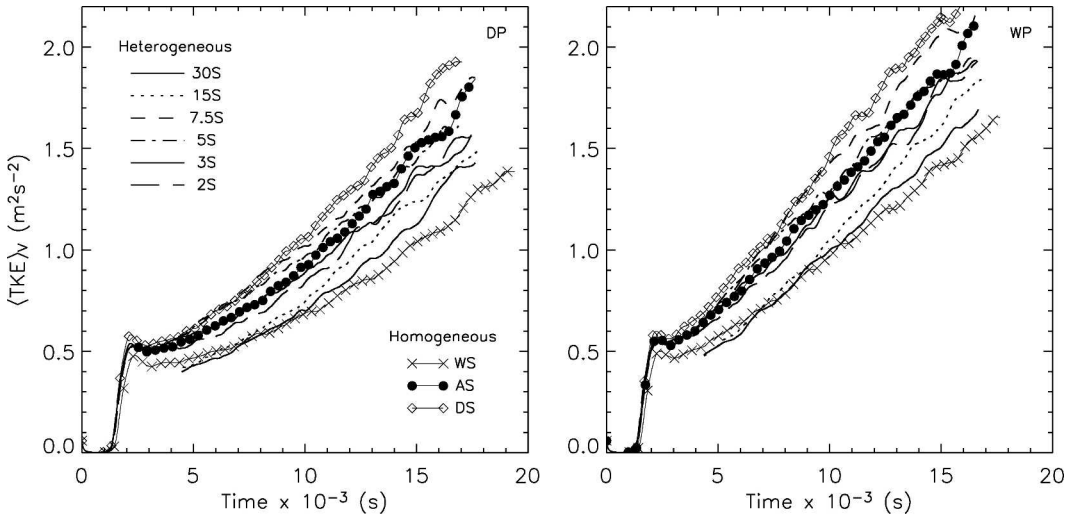

FIG. 2. The time variation of the volume-averaged turbulence kinetic energy, $\langle \mathrm{TKE} \rangle_V$.

tistics, x averages of phase-correlated variables are needed and this operation is denoted by brackets. For a single variable, $[f_p] = 0$ by definition and thus we show the x average of the absolute value $[|f_p|]$. We emphasize that x averages of phase products, for example the vertical flux $[w_p f_p]$ or variance $[f_p^2]$, are not equal to zero. Averages over the entire volume are denoted by $\langle\ \rangle_V$ and over the PBL depth and time as $\langle\ \rangle_{\mathrm{BL},t}$.

6. Results

a. Temporal variation

Letzel and Raasch (2003) observed persistent thermally induced oscillations in the convective boundary layer. With specified sinusoidal forcing (constant in time and space), their investigations revealed that in the presence of large-amplitude heterogeneous forcing (amplitude greater than 0.05 K m s^{-1}) oscillations in volume-averaged turbulence kinetic energy dominated the flow and persisted for multiple turnover times.

Investigation of the time variation of volume-averaged turbulent kinetic energy ($\langle \mathrm{TKE} \rangle_V$) from our simulations (Fig. 2) reveals no temporal oscillations. The average surface buoyancy flux predicted from our heterogeneously forced simulations is about 0.28 K m s^{-1} (Table 1) and the amplitude of the spatially varying component is about 0.03 K m s^{-1} (see section 6c). This may explain the absence of temporal oscillations in our simulations since Letzel and Raasch (2003) report no oscillations for forcing amplitudes below 0.05 K m s^{-1}. Figure 2 shows that the boundary-layer-averaged turbulence kinetic energy continually increases in time due to the continual growth of z_i in the absence of subsidence; the time variation of boundary-layer-averaged TKE normalized by time-varying w_*^2 remains constant for all DP (WP) cases after 10–11 (7–9) $\times$ 10^3 s (not shown). Therefore, at that point the turbulence in our simulations has reached statistical equilibrium with the forcing, that is, quasi-steady.

b. Heterogeneity-induced organized motions

The influence of the varying soil moisture is evident in the flow visualizations of vertical velocity and water vapor mixing ratio shown in Figs. 3 and 4. These figures illustrate how the presence or absence of soil moisture variation dramatically alters the turbulent motions in the PBL. Over the region of high soil moisture content (e.g., x = [0, 3.75], [7.5, 11.25], [15, 18.75], [22.5, 26.25] km, Fig. 4) convective plumes tend to be less vigorous compared to their counterparts in the region of low soil moisture content.

The shape of the inversion layer (i.e., the entrainment zone, around z = 1.3 to 1.5 km) is also altered by soil moisture heterogeneity. The local PBL depth is lower (higher) over the wet (dry) patches, which is consistent with recent observations that show large z_i variability from heterogeneous forcing under low wind conditions (Banta and White 2003). Entrainment of low water vapor mixing ratio is observed over the region of high soil moisture and entrained dry air extends all the way to the ground (cf. the second panels of Figs. 3 and 4). The average normalized mixing ratio in the domain is comparable for the two cases (not shown), but in the DP-7.5S case vertical averages reveal the lowest PBL mixing ratio exists over the wet soil.

To illustrate the organized motions and the influence of heterogeneity scale, Fig. 5 depicts phase-correlated horizontal and vertical velocity fields from cases DP-30S, DP-7.5S, and DP-3S. For case DP-7.5S ($\lambda/z_i \sim 4$), the phase-correlated vertical motions (middle right panel of Fig. 5) are most intense over the central core of the dry soil ($x/\lambda \sim 0.75$) with weaker sinking motion

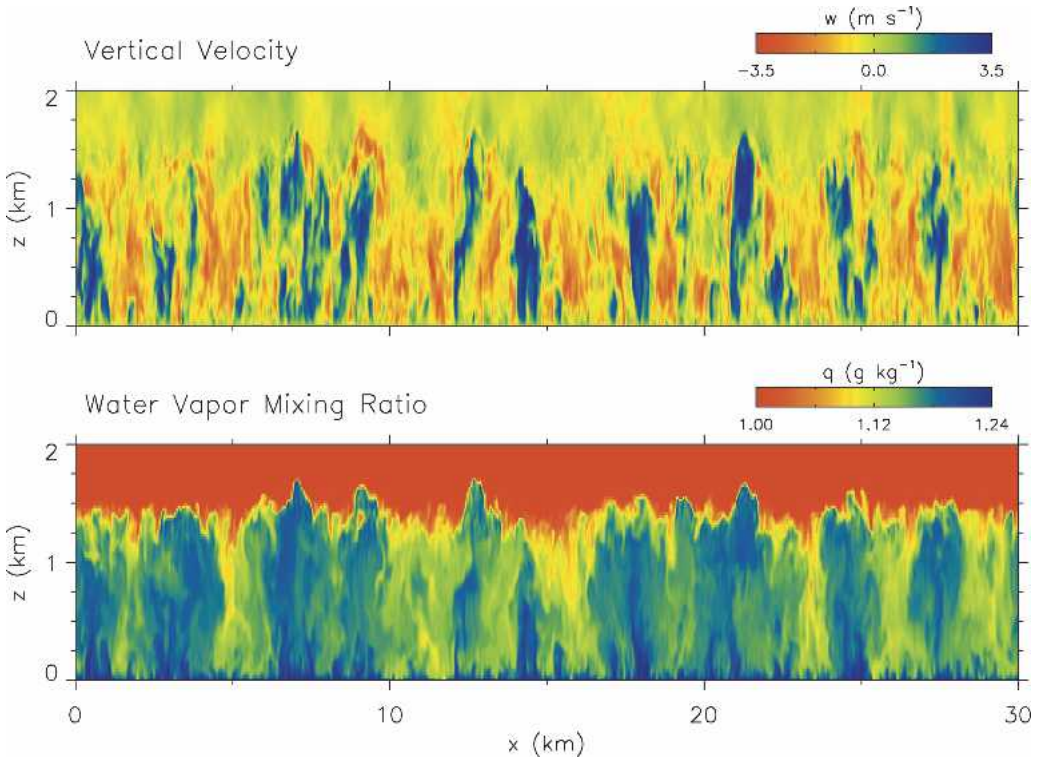

FIG. 3. Instantaneous two-dimensional slices of vertical velocity and water vapor mixing ratio at the first time step used in the averaging for case DP-AS.

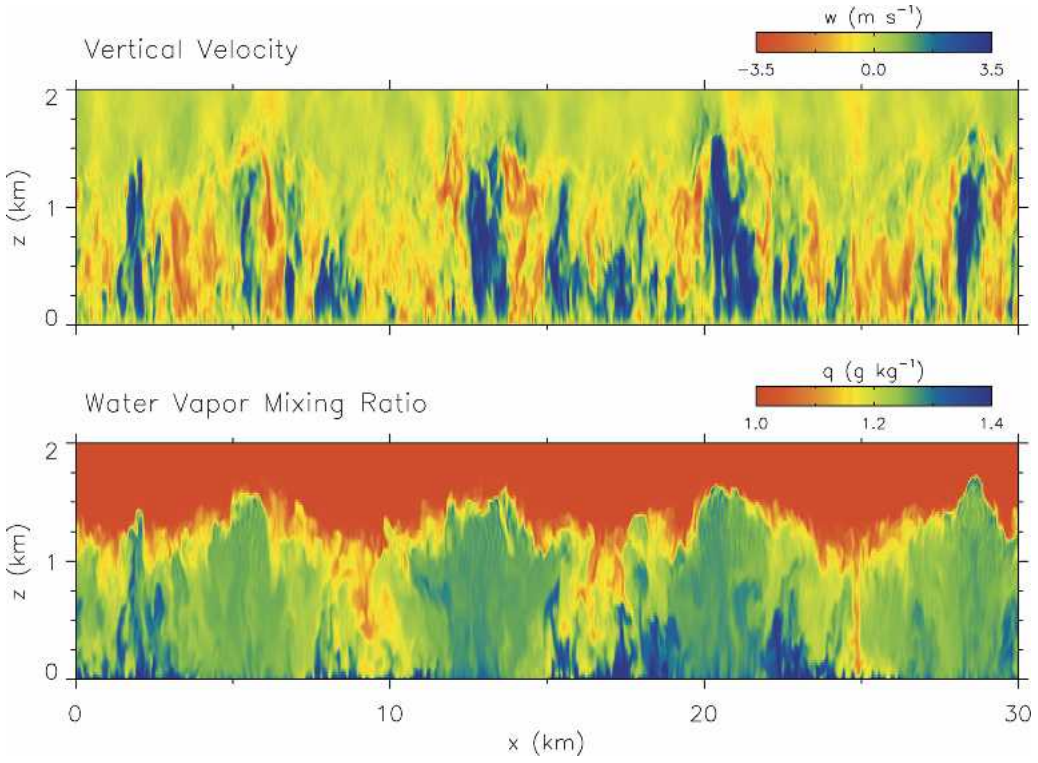

FIG. 4. As in Fig. 3 except for case DP-7.5S.

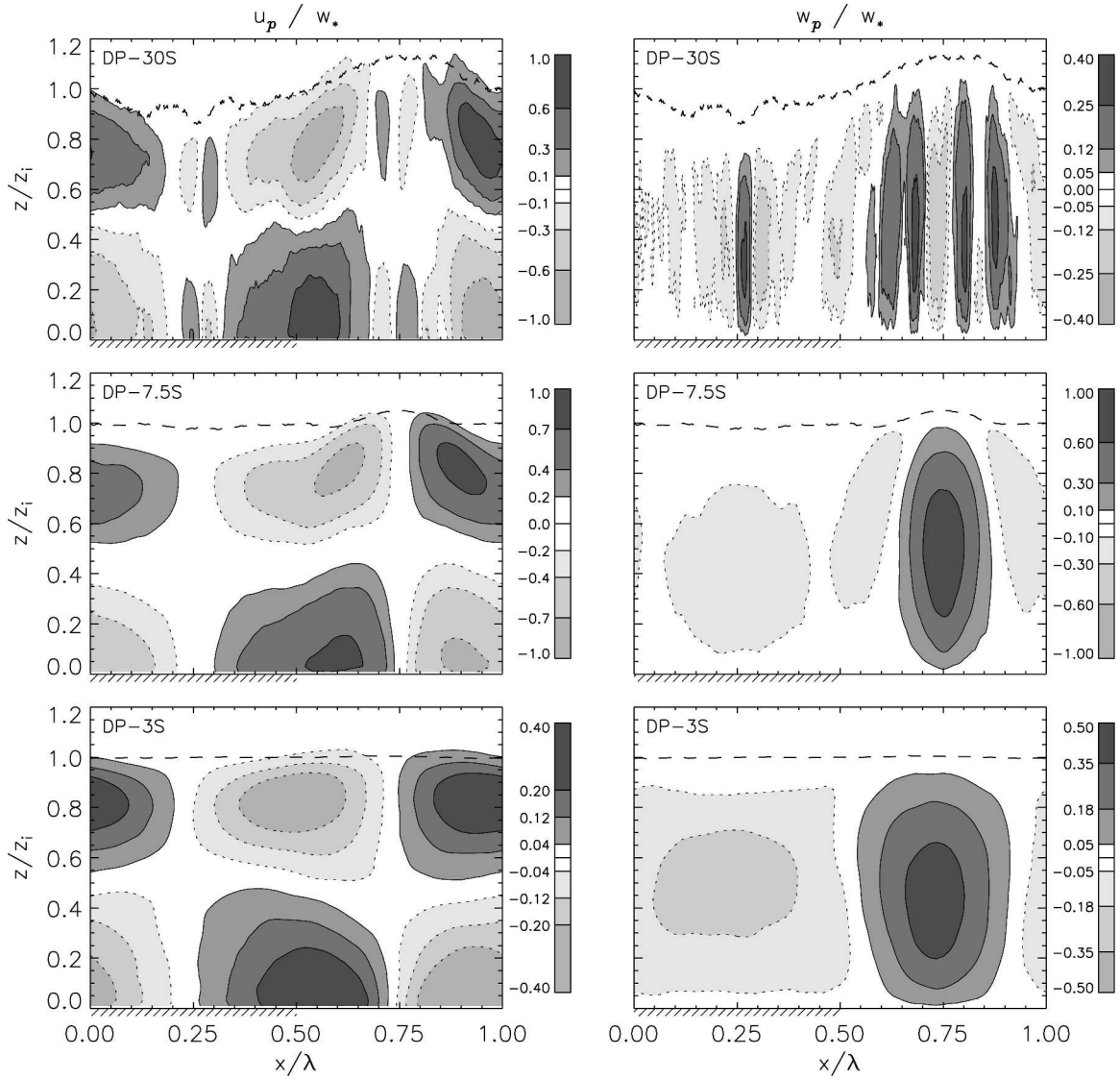

FIG. 5. (left) Normalized phase-correlated horizontal velocity (u_p/w_*) and vertical velocity (w_p/w_*) as a function of x/λ and z/z_i for cases (top) DP-30S, (middle) DP-7.5S, and (bottom) DP-3S. The dashed line is the phase-averaged boundary layer depth, z_{i_p}; dotted contours represent negative phase-correlated values; and the hatches demarcate the x/λ extent of the wet soil.

elsewhere. The rising motion is confined to 25% of the wavelength of the heterogeneity, centered about the middle of the dry patch. Based on the (u_p, w_p) flow fields, we picture the organized flow pattern as consisting of two counterrotating oblong cells that coincide over the center of the dry patch to form what appears to be a single region of rising motion. Near the ground, the fluid speed increases as air over the wet soil is brought toward the region of rising motion (middle left panel of Fig. 5), but is deflected upward before the stagnation point of horizontal velocity centered over the dry soil. The air approaching from both sides rapidly rises over the dry patch in a narrow core, subsequently being deflected outward by the inversion, and decreases in speed as it leaves the upwelling region. The return leg consists of weaker momentum fluid closing the return leg over a much broader area, but again centered over the wet patch. This picture is similar to the schematic presented by Segal and Arritt (1992) when discussing velocity patterns associated with mesoscale circulations.

Figure 5 shows that the intensity of these circulations varies with the scale of the heterogeneity. In cases with large heterogeneity, such as DP-30S ($\lambda/z_i \sim 18$), small-scale phase-correlated cells on a scale of (1 to 2)z_i, much smaller than the patch size, develop near the center of both the wet and dry patches far from the edge of the heterogeneity. Neither Avissar and Schmidt (1998) or Letzel and Raasch (2003) report the presence of these small-scale cells. These cells are not artifacts of

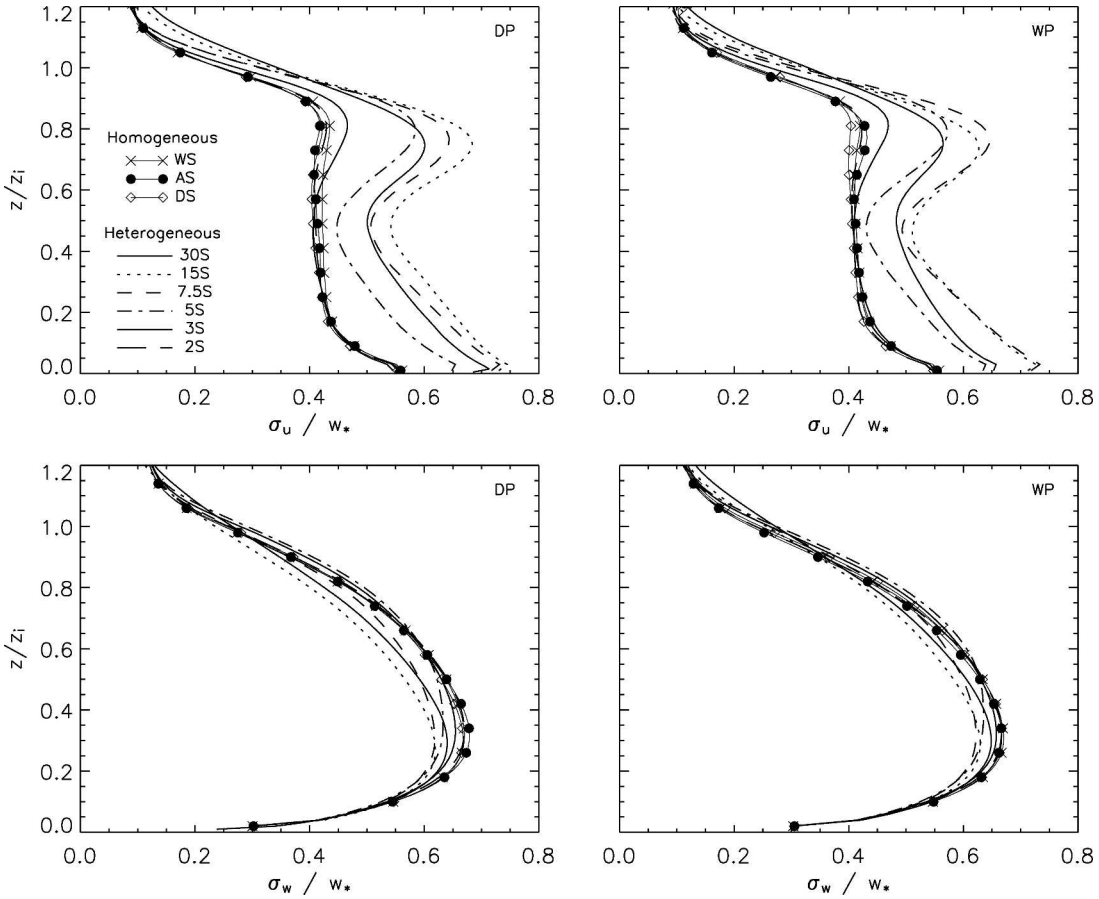

FIG. 6. Vertical profiles of normalized horizontal and vertical velocity standard deviation, $\sigma_u/w_* = (\langle u''^2\rangle + (2/3)\langle e\rangle)^{1/2}/w_*$ and $\sigma_w/w_* = (\langle w''^2\rangle + \frac{2}{3}\langle e\rangle)^{1/2}/w_*$, for both the DP and WP cases. Single lines represent heterogeneous cases. Lines with symbols represent homogeneous cases. The variable e is the subfilter-scale energy as predicted by the LES.

limited averaging in the 30S cases as sensitivity tests using averages over 9 and 21 turnover times reveal no difference in the magnitude or extent of the small-scale cells present in the center of the patches (not shown). Rather, the small-scale features are persistent flow structures and result from coupling with the land surface, which will be discussed further in section 6c.

The moisture state of the PBL does not vastly influence horizontal and vertical velocity fluctuations, as seen by comparing DP and WP cases in Fig. 6. We denote the normalized standard deviation of the horizontal velocity u as

$$\sigma_u/w_* = \left(\langle u''^2\rangle + \frac{2}{3}\langle e\rangle\right)^{1/2}/w_*$$

and for w as

$$\sigma_w/w_* = \left(\langle w''^2\rangle + \frac{2}{3}\langle e\rangle\right)^{1/2}/w_*.$$

Compared to the horizontally homogeneous cases, σ_u/w_* near the ground and entrainment zone follows a natural progression (increase, peak, and decrease) when transitioning from small-scale (2 km, $\lambda/z_i \sim 1$) to large-scale (30 km, $\lambda/z_i \sim 18$) heterogeneity (Fig. 6). The increase in horizontal velocity fluctuations, at both the ground and z_i, is consistent with the presence of nearly 2D organized circulations induced by the striplike heterogeneity and is also consistent with Avissar and Schmidt's (1998) results. The decrease of σ_u/w_* for large-scale heterogeneity is indicative of weaker organized circulations and will be discussed further in section 6c. For all cases, lateral velocity standard deviations (σ_v/w_*) are similar to each other (not shown).

The response of the velocity fluctuations to heterogeneity (Fig. 6) is strikingly similar to the expected change between shear- and buoyancy-driven PBLs. Moeng and Sullivan (1994) showed horizontal velocity variances to increase appreciably near the ground in the presence of a mean velocity shear. Therefore, free-convective PBLs in the presence of land surface heterogeneity are somewhat analogous to free-convective PBLs over homogeneous surfaces but with strong shear effects.

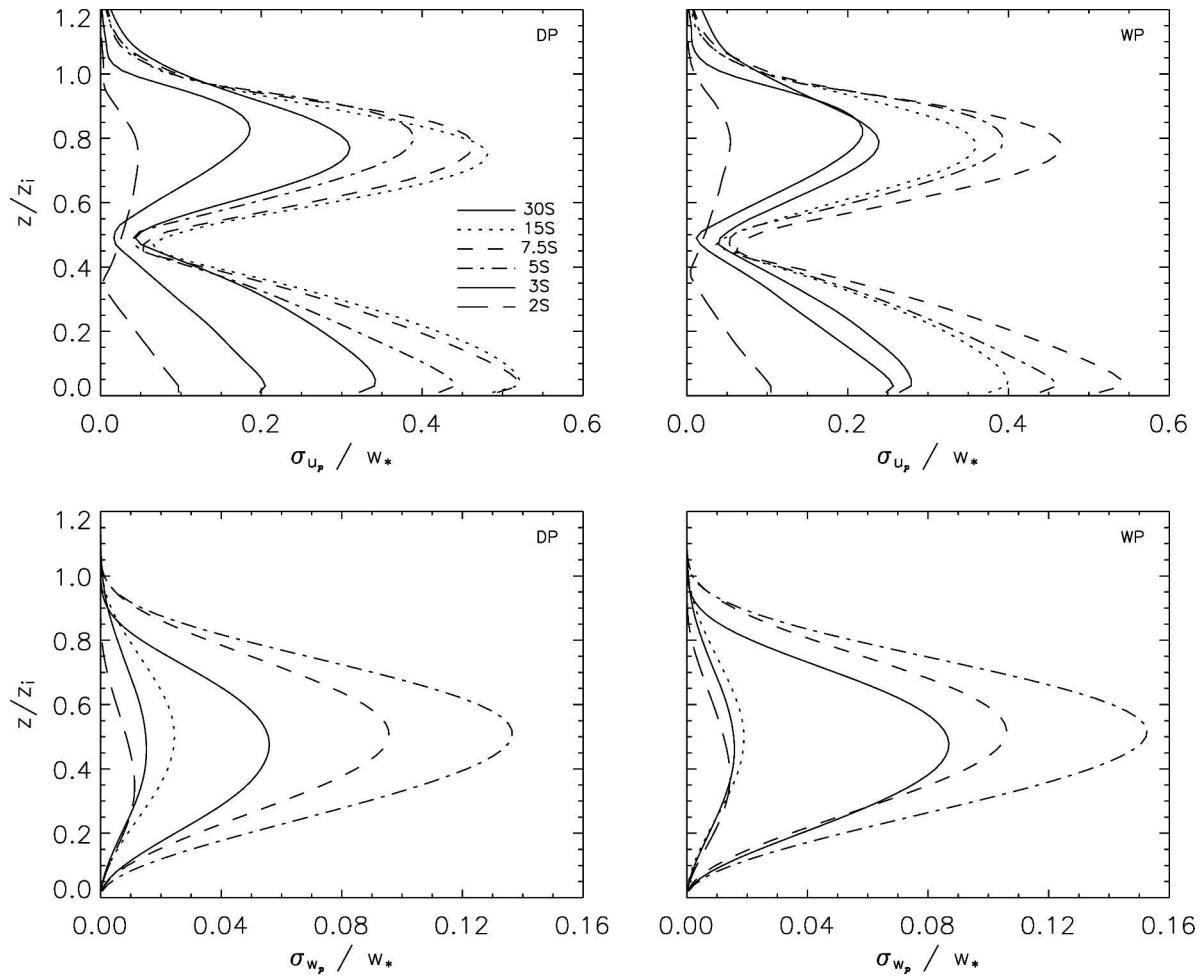

FIG. 7. The normalized x average of the root-mean-square phase-correlated horizontal velocity ($[u_p^2]^{1/2}/w_*$) and vertical velocity ($[w_p^2]^{1/2}/w_*$) for all cases with heterogeneity. (left) DP cases and (right) WP cases.

The intensity of the organized motions and their variation with heterogeneity scale can be quantified by examining phase-correlated velocity components

$$(\sigma_{u_p}, \sigma_{w_p})/w_* = ([u_p^2]^{1/2}, [w_p^2]^{1/2})/w_*$$

(see Fig. 7).[2] Figure 6 presents the heterogeneity-induced modification to the total turbulence, while Fig. 7 depicts the contribution to the fluctuations from the heterogeneity-induced organized motion. The heterogeneity-induced motions contribute more to fluctuations in horizontal velocity than vertical velocity (Figs. 6 and 7). The influence of heterogeneity does not vary linearly as λ/z_i varies from 1 to 18. The most intense patch-induced motion occurs for scales $4 < \lambda/z_i < 9$. For these scales the σ_{u_p}/w_* increase to about $0.5w_*$, compared to zero for the homogeneous cases, while w_p increases to about $0.15w_*$ for $\lambda/z_i \sim 3$. Meanwhile, for scales $\lambda/z_i > 9$ or $\lambda/z_i < 3$, the magnitudes of σ_{u_p}/w_* and σ_{w_p}/w_* become smaller as λ/z_i increases or decreases, respectively. In other words, there appears to be an optimum scale of heterogeneity λ/z_i between 4 and 9 that generates the most intense organized motions. Comparing the right and left panels of Fig. 7 shows no significant effect on the patch-induced velocity variances due to the moisture content in the PBL (i.e., between DP and WP cases).

Roy and Avissar (2000) find that if the horizontal pressure gradient induced by the heterogeneity exceeds the buoyant forcing the atmosphere is dominated by "rolls". If the balance switches such that the buoyant forcing dominates the pressure gradient, then the rolls are typically broken down into small-scale plumes, which may explain the features seen in our cases with small λ/z_i.

To elaborate on Roy and Avissar's (2000) comments regarding the horizontal pressure gradient, Fig. 8 presents the normalized phase-averaged pressure (p_p/w_*^2)

[2] Recall that by construction, the x average of a phase-correlated variable is zero, thus we consider the root-mean-square of the quantity.

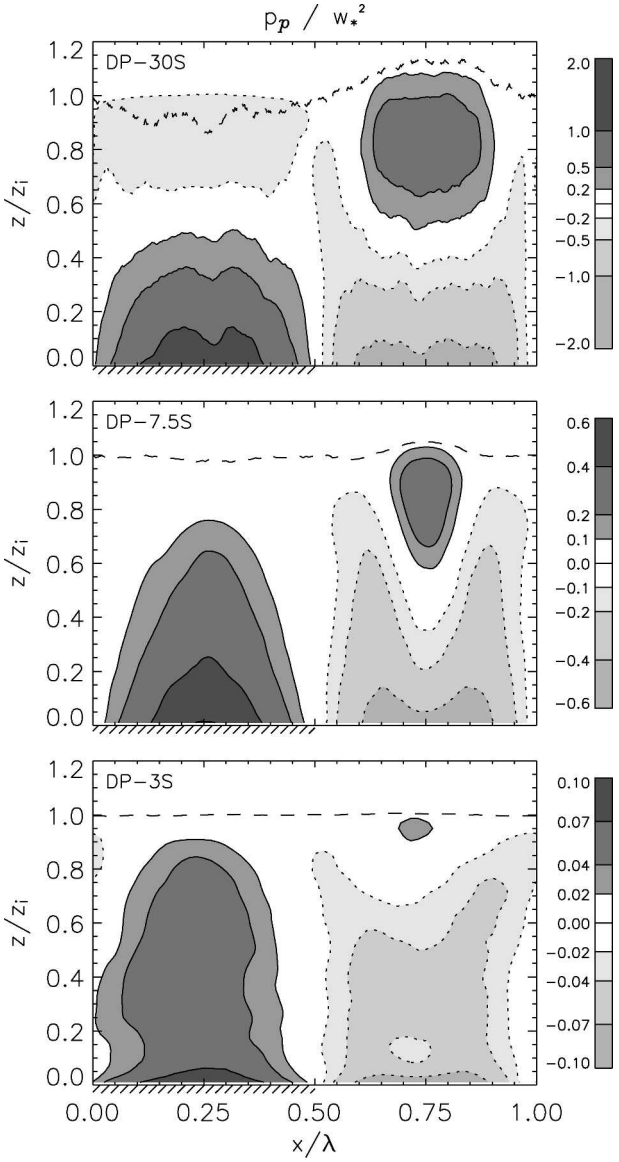

FIG. 8. Normalized phase-correlated pressure (p_p/w_*^2) as a function of x/λ and z/z_i for cases (top) DP-30S, (middle) DP-7.5S, and (bottom) DP-3S. All markings on the figures are the same as those defined in Fig. 5. Note the change in magnitude for the different cases.

for three cases; p_p is interpreted as the pressure induced by the heterogeneity. For all cases, relative high pressure is found at the bottom of the descending leg of the circulations (middle of the wet patch), relatively low pressure below the rising motion, and relatively high pressure again at the uppermost reach of the rising motion (middle of the dry patch). Taking the difference between the maximum and minimum p_p values at the lowest model level and dividing by the actual distance between them, we can estimate the heterogeneity-induced pressure gradients as shown in Table 2. The near-surface pressure difference is largest for the large-scale heterogeneity (30S), but is separated by a larger distance than the 7.5S cases (which exhibit the largest pressure gradient), and hence the pressure gradient in the 30S cases is smaller than the 7.5S cases.

TABLE 2. Maximum near-surface horizontal pressure gradient ($\partial p_p/\partial x$) normalized by (w_*^2/z_i).

Case	$(\partial p_p/\partial x)^*(z_i/w_*^2)$
DP-30S	0.27
DP-15S	0.51
DP-7.5S	0.58
DP-5S	0.54
DP-3S	0.21
DP-2S	0.20
WP-30S	0.27
WP-15S	0.42
WP-7.5S	0.62
WP-5S	0.40
WP-3S	0.25
WP-2S	0.20

c. *Surface fluxes*

Since the incoming solar radiation is the only external input of energy, all surface fluxes are dynamically determined through the LES–LSM coupling. These fluxes vary with time and space based upon atmospheric demand and soil availability. Figure 9 depicts the normalized phase-averaged sensible, latent, and soil heat fluxes for cases DP-30S, DP-7.5S, and DP-3S. Patch-averaged surface fluxes for case DP-3S ($\lambda/z_i \sim 1.7$) are nearly constant across both the wet and dry sides (dashed curves in Fig. 9) as the organized motions in this case are of weak intensity. Cases with stronger organization exhibit notable influence of the patch-induced motions on the surface sensible, latent, and soil heat fluxes.

Over the wet soil (left panels) the sensible and latent heat fluxes are at a minimum in the center of the patch, with relative maxima at the patch edges. As shown in Fig. 5, the patch centers correspond to the stagnation points of the near-surface horizontal winds associated with the patch-induced circulation, leading to minimum surface fluxes at these locations. Patch-induced horizontal winds accelerate toward the patch edges, thereby enhancing the surface exchange of heat and moisture and hence reduce the amount of heat going into warming the soil (i.e., the reduction in $\tilde{G}/\langle G\rangle$ at the patch edges). Over the dry soil (right column, Fig. 9) the phase-correlated surface sensible and latent heat fluxes are again minimized at the center of the patch, with maximum fluxes near $x/\lambda = 0.6$ and 0.9, instead of at the patch edges as observed on the wet side. The location of these maxima results from the peak in phase-correlated horizontal velocities (see Fig. 5). A similar trend is seen in the WP cases (not shown).

The magnitude and spatial (x) asymmetry of the surface fluxes (Fig. 9) highlights the importance of the fully

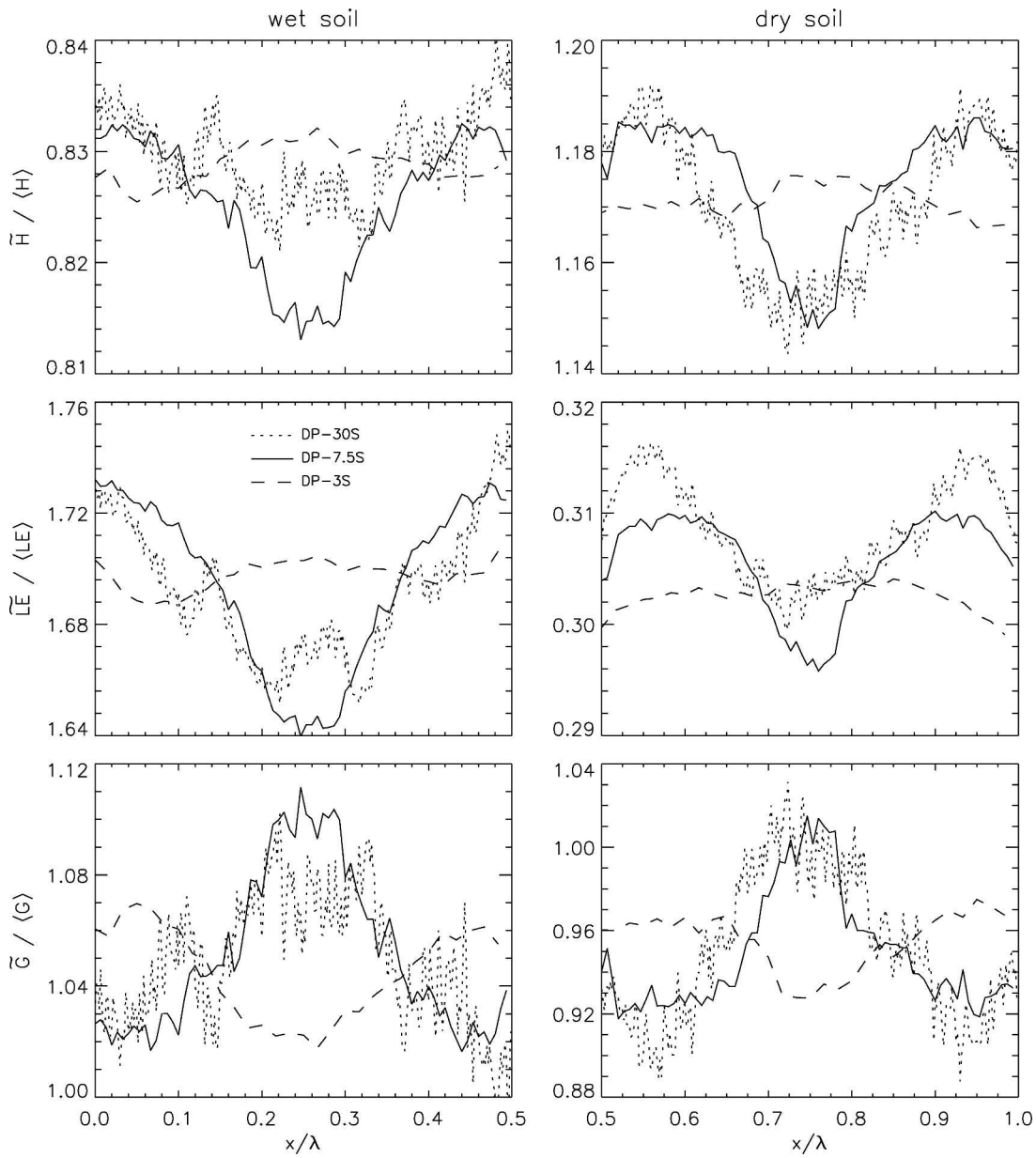

FIG. 9. Phase-averaged sensible ($\tilde{H}$), latent ($\widetilde{LE}$), and soil ($\tilde{G}$) heat fluxes normalized by their respective horizontal- and time-averaged quantity ($\langle H\rangle$, $\langle LE\rangle$, $\langle G\rangle$) for cases DP-30S (dotted line), DP-7.5S (solid line), and DP-3S (dashed line). (left) Wet and (right) dry side of the heterogeneity.

coupled system, which allows the surface fluxes to respond naturally to the atmospheric circulations. Most previous studies investigating the influence of heterogeneity impose a sinusoidal surface heat flux with the peaks and valleys of the forcing coincident with the center of the patch (e.g., Avissar and Schmidt 1998; Letzel and Raasch 2003), fixed at $x/\lambda = 0.25$ and 0.75. An advantage of the coupled system is that it allows the soil to dry and cool at the edge of the heterogeneity, a feature that cannot be captured with either fixed surface flux forcing (e.g., Avissar and Schmidt 1998; Letzel and Raasch 2003) or with specified surface temperature and moisture (e.g., Kustas and Albertson 2003). The stronger the organized motion, the greater the cooling and drying of the soil; this results not only because of increased winds, but also because of dry air entrained aloft being brought down over the wet surface (see Fig. 4).

The coupled land surface–atmosphere system appears to select a preferred (or optimum) scale ($4 \leq \lambda/z_i \leq 9$). In the discussion of Fig. 5, it was noted that in case DP-30S ($\lambda/z_i \sim 18$), the patch-scale organized cir-

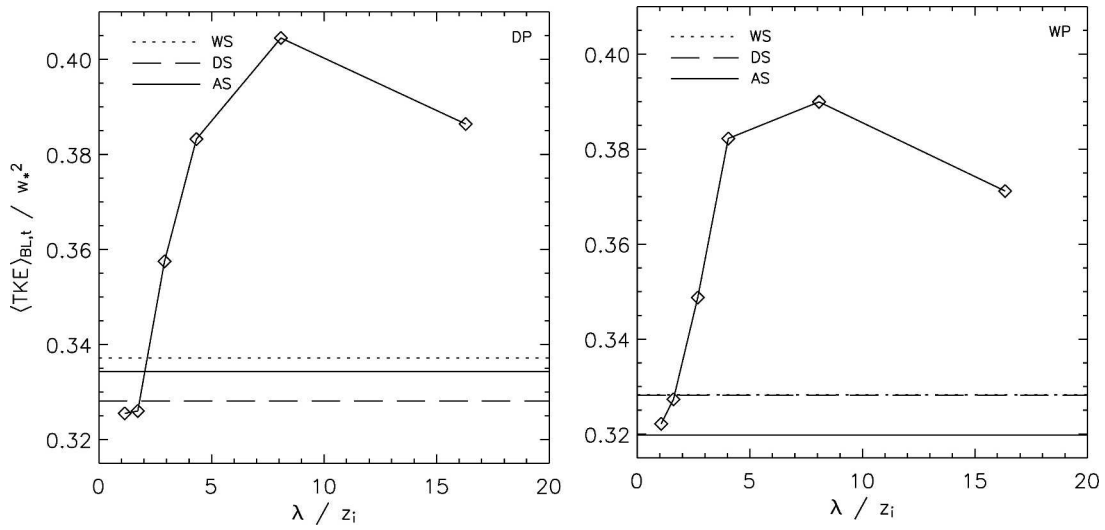

FIG. 10. Boundary layer and time-averaged TKE normalized by w_*^2 vs the normalized heterogeneity wavelength (λ/z_i) for both the DP and WP cases. The line with symbols represents the heterogeneous soil cases. The solid, dashed, and dotted lines with no symbols are the homogeneous soil cases.

culations did not penetrate to the center of the patches and rising (sinking) motion persists in the center of the wet (dry) patches. These small-scale cells persist because at this large heterogeneity scale ($\lambda/z_i \sim 18$), the surface fluxes peak at regions far from the patch center (Fig. 9), and the horizontal gradient of the surface fluxes across each individual patch (e.g., from the peaks at $x/\lambda \sim 0.6$ and 0.9 to the minimum at $x/\lambda \sim 0.75$) is comparable to the large-scale gradient across λ (not shown). In cases with smaller-scale heterogeneity (e.g., DP-7.5S, $\lambda/z_i \sim 4$), although the surface fluxes also exhibit flux peaks over both the wet and dry patches, the flux gradient across λ is notably larger than the gradient across the individual patches (not shown). Therefore, in case DP-30S ($\lambda/z_i \sim 18$) persistent small-scale phase-correlated cells coexist with the patch-scale organized circulations. The small-scale cells in the patch center also persist in the WP-30S case.

d. Heterogeneity influence on bulk statistics

1) TURBULENCE KINETIC ENERGY

Total turbulence kinetic energy (averaged over the PBL and time, $\langle\ \rangle_{\mathrm{BL},t}$) responds sensitively to land surface heterogeneity (Fig. 10). Heterogeneity at scales larger than twice the depth of the boundary layer ($\lambda/z_i > 2$) increases the PBL- and time-averaged turbulent kinetic energy; which is consistent with the findings of both Avissar and Schmidt (1998) and Letzel and Raasch (2003), who found increased volume averaged TKE for heterogeneity scales larger than z_i, but TKE remains similar to that in the homogeneous cases for small-scale heterogeneity. For the $\lambda/z_i \sim 18$ cases, however, the TKE decreases due to weaker organized circulations as shown in Fig. 5. The TKE is most enhanced for cases DP-15S and WP-15S ($\lambda/z_i \sim 9$), which is larger by 14% and 19%, respectively, than that of the horizontally homogeneous cases.

2) ENTRAINMENT RATES

As is apparent from Figs. 3 and 4, under free convection, heterogeneous soil moisture induces organized motions that alter PBL dynamics and the structure of the PBL top interface. Therefore, it is anticipated that heterogeneity can potentially modify the growth rate of the PBL. However, Fig. 11 shows that heterogeneity or the initial PBL moisture content only slightly modify the entrainment rates ($w_e = \partial\langle z_i\rangle/\partial t$) compared to the homogeneous cases. Heterogeneity scales on the order of the PBL depth tend to decrease normalized entrainment rates compared to the AS cases, although this decrease is only 5.6 (5.5) % for the DP (WP) cases. Heterogeneity scales of 9 (5) times z_i slightly increase the entrainment rates for the DP (WP) cases, but this increase is only 5.3 (3.8) % compared to the AS cases, respectively; these entrainment rates are also slightly higher than the homogeneous dry soil (DS) cases. Although some previous LES studies have suggested increased entrainment rates due to heterogeneity (e.g., Avissar and Schmidt 1998), our study suggests little heterogeneity influence on w_e.

The combined results presented in Figs. 10 and 11 indicate that the entrainment rate is not directly proportional to TKE for heterogeneous surface conditions. In free-convective PBLs, we show that TKE is strongly affected by surface-induced circulations, while the entrainment rate appears to be more dependent on the rate of surface heating than the heterogeneity.

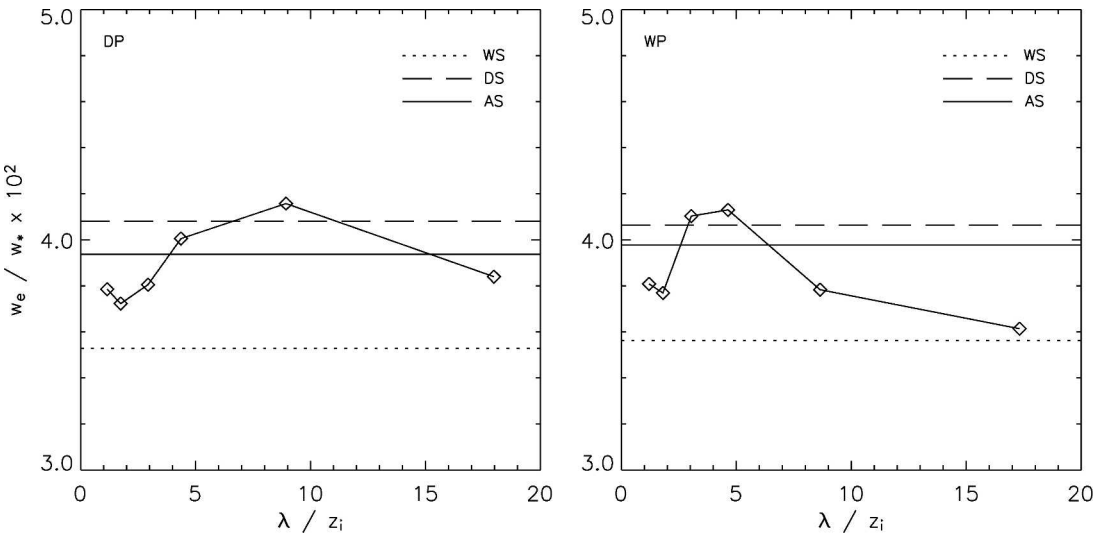

FIG. 11. Normalized entrainment rates (w_e/w_*) vs the normalized heterogeneity wavelength (λ/z_i) for both the DP and WP cases. The line with symbols represents the heterogeneous soil cases. The solid, dashed, and dotted lines with no symbols are the homogeneous soil cases.

e. Heterogeneity influence on vertical scalar fluxes

1) THE TOTAL FLUX

Heterogeneity has small impact on the total normalized vertical flux of either virtual potential temperature or water vapor mixing ratio for both the DP and WP PBLs (Figs. 12 and 13). Normalized profiles of vertical virtual potential temperature flux are linear through the PBL for all cases, which confirms that 1) our LES solutions have reached quasi-steady conditions and 2) Letzel and Raasch's (2003) speculation that Avissar and Schmidt's (1998) heterogeneity-induced modifications to the vertical potential temperature flux profiles are a result of limited averaging. Most of the profiles have a minimum flux ratio (just below z_i) of about -0.12, which is smaller than the traditional value of -0.2 (Deardorff 1979). The entrainment to surface buoyancy flux ratio for the 15S and 30S cases have an even smaller magnitude. We attribute this smaller flux ratio to a weak capping inversion that results in a thicker entrainment zone. Lilly (2002) also suggests that averaging in a surface-following coordinate system should eliminate the smearing of the flux values induced by averaging across the undulating interface. The

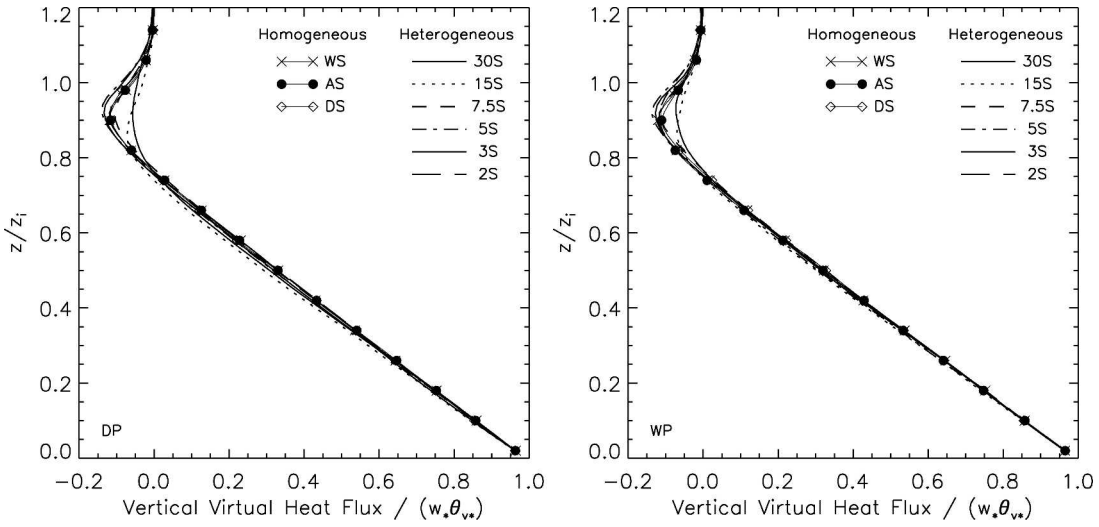

FIG. 12. Vertical profiles of normalized vertical flux of virtual potential temperature $(\langle w''\theta_v'' + \tau_{w\theta_v}\rangle)/(w_*\theta_{v*})$ for both the DP and WP cases. Lines by themselves represent heterogeneous cases. Lines with symbols represent homogeneous cases; $\tau_{w\theta_v}$ is the SFS vertical virtual potential temperature flux predicted by the SFS model.

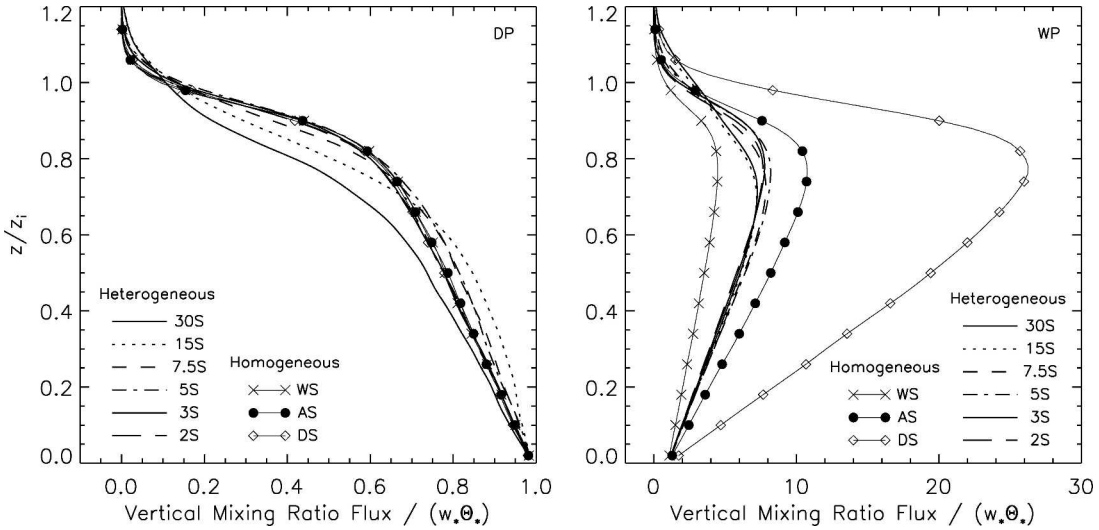

FIG. 13. Vertical profiles of normalized vertical flux of water vapor mixing ratio $(\langle w''q'' + \tau_{wq}\rangle)/(w_*\Theta_*)$ for both the DP and WP cases. Lines by themselves represent heterogeneous cases. Lines with symbols represent homogeneous cases; τ_{wq} is the SFS vertical mixing ratio flux predicted by the SFS model.

differences among the three homogeneous cases seen in Fig. 13 is due to the different jump conditions across the entrainment interface resulting from different surface latent heat fluxes.

2) THE PATCH-INDUCED CONTRIBUTION

Although the total vertical fluxes show small variability in the presence of heterogeneity, different mechanisms are responsible for the total flux. Figures 14 and 15 present the contributions from the phase-correlated (patch induced) and background turbulence to the total scalar flux for 30S, 7.5S, and 3S cases. The total turbulent fluxes for virtual potential temperature and moisture are $\langle w''\theta_v'' + \tau_{w\theta v}\rangle/\theta_{v*}$ and $\langle w''q'' + \tau_{wq}\rangle/\Theta_*$, where the double primed quantities are resolved fluctuations and τ is the SFS flux.

Previous studies using mesoscale models with parameterized ensemble-mean turbulence (e.g., Zeng and Pielke 1995; Seth and Giorgi 1996) find that entrainment largely results from the mesoscale organized motions. However, our turbulence-resolving LES reveals that under heterogeneous forcing background turbulence is (on average) responsible for entrainment, as indicated in Figs. 14 and 15 by the relative importance of the background turbulence (dashed curves) compared to the phase-correlated fluxes (dotted curves) within the entrainment zone (e.g., $0.95 \leq z/z_i \leq 1.05$).

In the DP-7.5S case ($\lambda/z_i \sim 4$), vertical water vapor fluxes are dominated by the heterogeneity-induced organized motions in the upper half of the PBL (middle left panel of Fig. 15), while in the WP-7.5S case the heterogeneity-induced organized motions contribute most of the flux through the bulk of the PBL (middle right panel of Fig. 15). Averaged across the heterogeneity, $[w_p q_p]/(w_*\Theta_*)$ in case DP-7.5S contributes a maximum of 68% to the total flux at $z/z_i \sim 0.7$, while in the WP-7.5S case the phase-correlated component contributes almost 100% to the total flux throughout the PBL. The difference between DP and WP cases is largely due to the moisture gradient across the entrainment interface. In the WP case, the organized motions intensify the moisture jump across the inversion over the dry soil (not shown), which enhances the contribution of the organized motions to the vertical flux of q. For both DP-30S and DP-3S cases, the patch-induced component of the vertical mixing ratio flux is nearly zero, while both WP-30S and WP-3S show moderate contributions (Fig. 15).

3) IMPACT ON POINT MEASUREMENTS

Vertical scalar fluxes are one of the primary quantities deduced from observations collected from fixed towers and platforms. Most often, vertical scalar flux is not directly measured but is instead computed from independent measurements of vertical velocity and the scalar of interest. Vertical flux estimates thus depend crucially on accurate vertical velocity measurements. In the field, sensors are imperfectly deployed and observationalists typically apply tilt corrections that force time-averaged w measurements (at a point) to zero (e.g., Dyer 1981; Baldocchi et al. 1988; Berger et al. 2001; Finnigan et al. 2003). For example, Dyer (1981) notes that estimates of vertical momentum flux are corrected by about 14% per degree of tilt, while Baldocchi et al. (1988) reports a smaller scalar flux correction (about 3% per degree of tilt). Kanda et al. (2004) and others have suggested that forcing time-averaged w to zero can bias point measurements even under horizon-

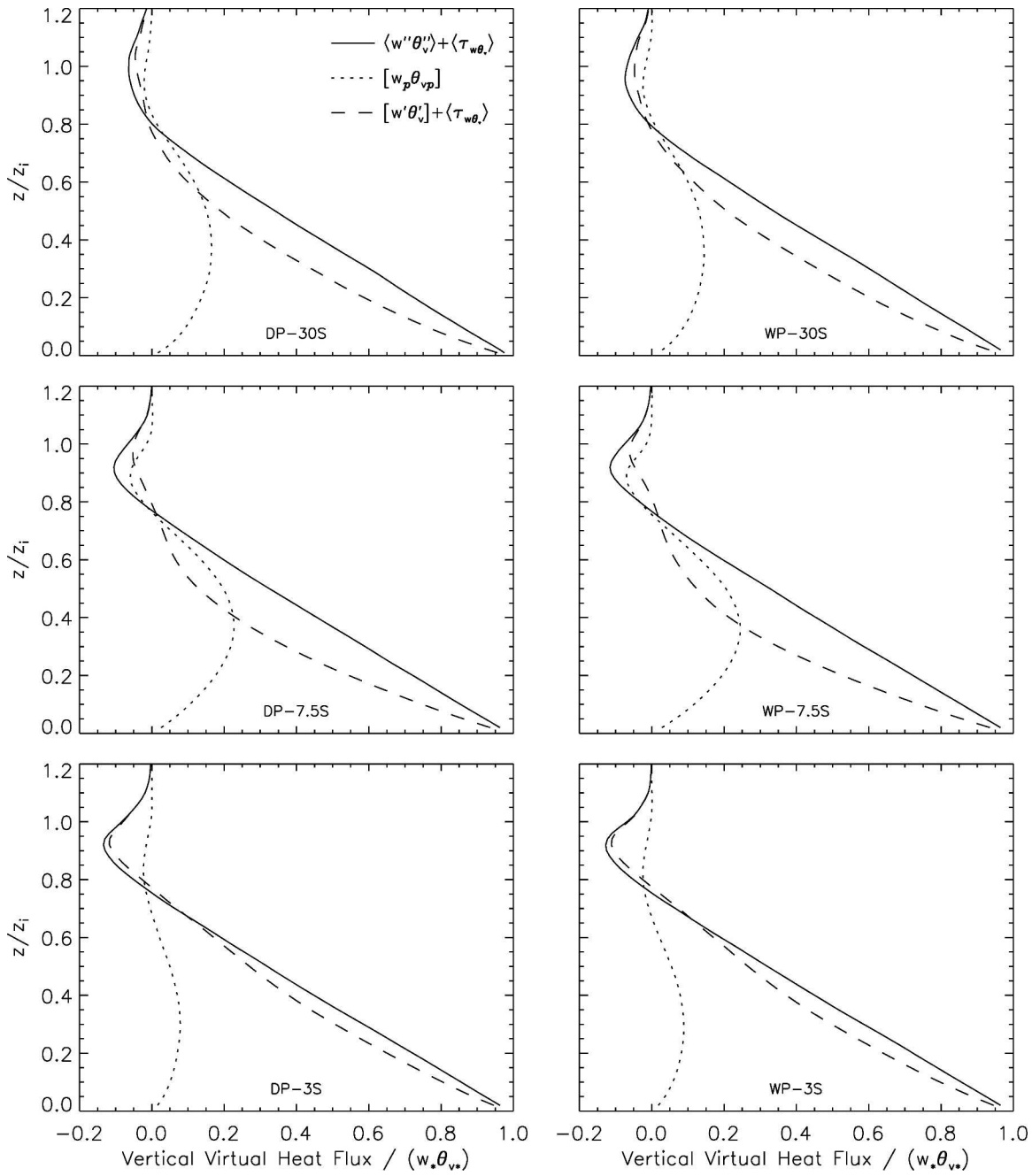

FIG. 14. Vertical profiles of normalized total virtual heat flux $(\langle w''\theta_v''\rangle + \langle\tau_{w\theta_v}\rangle)/(w_*\theta_{v*})$, the phase-correlated virtual heat flux $[w_p\theta_{vp}]/(w_*\theta_{v*})$, and background turbulent virtual heat flux $(\langle w'\theta_v'\rangle + \langle\tau_{w\theta_v}\rangle)/(w_*\theta_{v*})$ for six cases. (left) DP cases and (right) WP cases; and (top) 30S cases, (middle) 7.5S cases, and (bottom) 3S cases.

tally homogeneous forcing due to organized turbulent structures. The practice of forcing average vertical velocity to zero becomes especially uncertain in the presence of surface heterogeneity (e.g., Finnigan et al. 2003). The question we wish to address with our simulations is: what are the possible consequences of assuming time average $w = 0$ at a fixed point for scalar flux in the presence of heterogeneous surface conditions?

To elucidate the importance of the heterogeneity-induced organized motions on point measurements, we compare three vertical profiles for the DP-7.5S case in Fig. 16: 1) the total flux, 2) the background turbulence contribution to this total flux, and 3) fluxes calculated from time averages at a point. The horizontal locations chosen here are $x/\lambda = 0$ or 1, 0.25, 0.5, 0.75. The filled circles represent y and time average (denoted as $\langle\rangle_{y,t}$) of

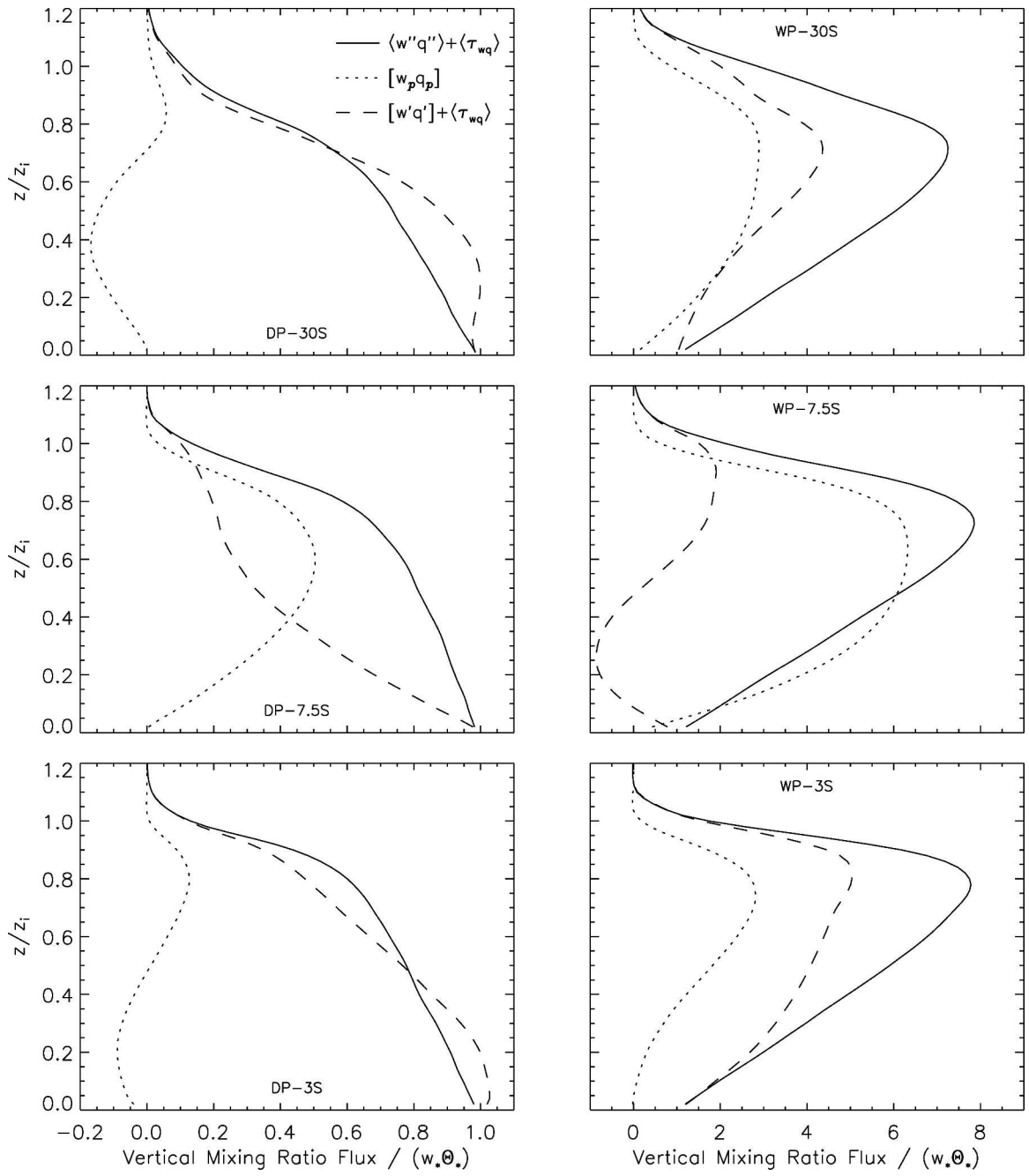

FIG. 15. Vertical profiles of normalized total vertical mixing ratio flux $(\langle w''q''\rangle + \langle \tau_{wq}\rangle)/(w_*\Theta_*)$, the phase-correlated mixing ratio flux $[w_p q_p]/(w_*\Theta_*)$, and background turbulent mixing ratio flux $([w'q'] + \langle \tau_{wq}\rangle)/(w_*\Theta_*)$ for six cases. (left) DP cases and (right) WP cases; and (top) 30S cases, (middle) 7.5S cases, and (bottom) 3S cases.

the background turbulence component of the total vertical virtual potential temperature flux [denoted with a single prime $'$ as defined in Eq. (1)]. The hatched areas represent plus and minus one standard deviation of these y- and time-averaged quantities. The time-averaged profiles are calculated from fixed point data saved every ten time steps, averaged over the same length of time as the ensemble averaged data (4 to 10 turnover times). In this case, the fluxes are calculated using the following rule, $\{w^\circ f^\circ\} = \{wf\} - \{w\}\{f\}$, where f is any scalar and braces represent a time average at a fixed point over 4 to 10 turnover times and the degree symbol is the deviation from that time average. Notice that the time-averaged background (turbulent) fluxes are in good agreement with their counterparts obtained using both spatial and temporal averages.

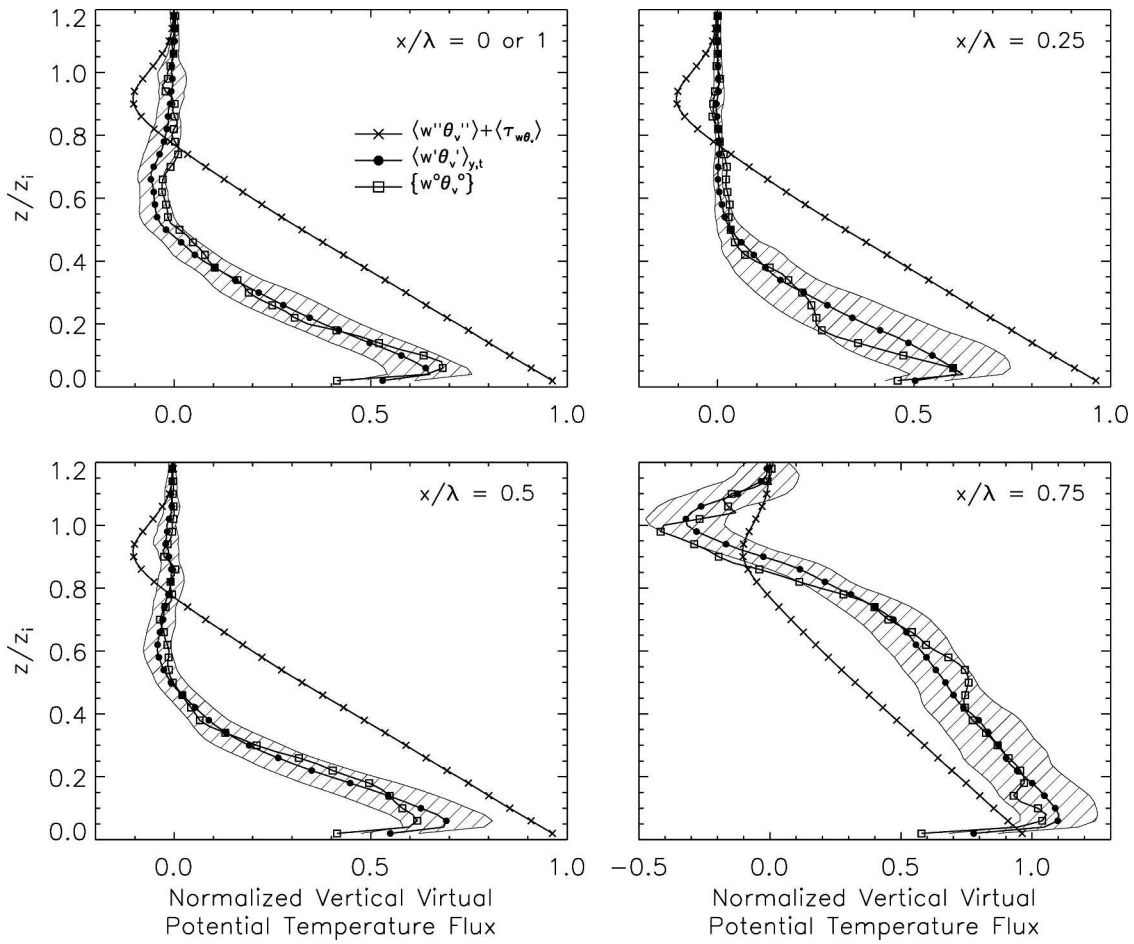

FIG. 16. Vertical profiles of normalized vertical virtual potential temperature flux for case DP-7.5S. The × profile represents the total flux, $(\langle w''\theta_v''\rangle + \langle\tau_{w\theta_v}\rangle)/(w_*\theta_{v*})$. The ● profile presents the background turbulent contribution, $\langle w'\theta_v'\rangle_{y,t}/(w_*\theta_{v*})$, and the hatch marks demarcate ±1 standard deviation of $\langle w'\theta_v'\rangle_{y,t}/(w_*\theta_{v*})$ from the y average. The □ profile is the time average at each x/λ and z/z_i location at $y = 2.5$ km. Locations x/λ = (top left) 0 or 1, (top right) 0.25, (lower left) 0.5, and (lower right) 0.75. See the discussion in section 6e(3) for further explanation of how these quantities are calculated.

Time-averaged vertical virtual potential temperature fluxes obtained at individual x locations in a free-convective PBL with $\lambda/z_i \sim 4$ heterogeneity differ significantly from the total vertical flux (Fig. 16). The magnitude and sign of the difference depends on the x/λ and z/z_i location of the point measurement. At the center of the wet soil ($x/\lambda = 0.25$), point flux measurements underestimate the vertical virtual potential temperature flux throughout the free-convective PBL. While over the center of the dry patch ($x/\lambda = 0.75$), the point measurements overestimate the vertical virtual potential temperature flux. For example, under free convective conditions a time-averaged point measurement at $x/\lambda = 0.25$ and $z/z_i = 0.1$ would underestimate the vertical flux of virtual potential temperature by about 45%, while the same measurement at $x/\lambda = 0.75$ would overestimate the flux by about 20%.

Again for DP-7.5S, simulated point measurements of vertical mixing ratio flux are given in Fig. 17. Over the wet patch ($x/\lambda = 0.25$), below $z/z_i \sim 0.4$, point measurements overestimate the vertical flux, while above this height such measurements underestimate the flux. Over the dry patch ($x/\lambda = 0.75$) point measurements dramatically underestimate the vertical mixing ratio flux below $z/z_i \sim 0.8$, while above this level point measurements overestimate the entrainment of dry air from above. To quantify the influence near the surface, under free convective conditions a time-averaged point measurement at $x/\lambda = 0.25$ and $z/z_i = 0.1$ would overestimate the vertical flux of water vapor mixing ratio by about 3%, while the same measurement at $x/\lambda = 0.75$ would underestimate the flux by about 60%.

We caution the reader regarding the conclusions made from Figs. 16 and 17 for the following reasons: 1) these results are representative for a single heterogeneity scale ($\lambda/z_i \sim 4$) and 2) these conclusions apply only to convective PBLs with no mean wind. For PBLs with mean wind, point measurements assume that numerous energy-containing eddies are sampled over the averaging time period (Kaimal and Finnigan 1994). Since our

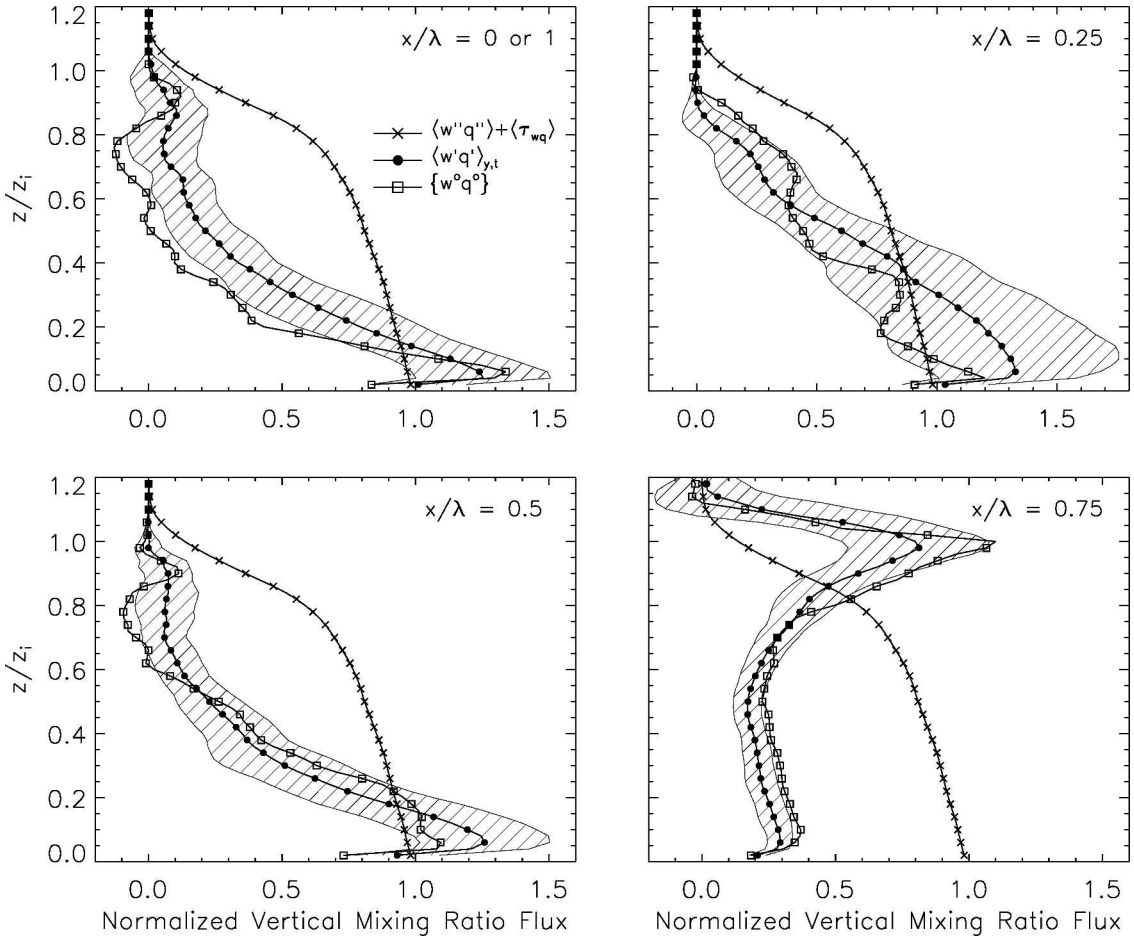

FIG. 17. Vertical profiles of normalized vertical water vapor mixing ratio flux for case DP-7.5S. The x profile represents the total flux, $(\langle w''q''\rangle + \langle \tau_{wq}\rangle)/(w_*\Theta_*)$. The ● profile presents the background turbulent contribution, $\langle w'q'\rangle_{y,t}/(w_*\Theta_*)$, and the hatch marks demarcate ±1 std dev of $\langle w'q'\rangle_{y,t}/(w_*\Theta_*)$ from the y average. The □ profile is the time average at each x/λ and z/z_i location at y = 2.5 km. Locations x/λ = (top left) 0 or 1, (top right) 0.25, (lower left) 0.5, and (lower right) 0.75. See the discussion in section 6e(3) for further explanation of how these quantities are calculated.

simulations are of free convection, the point measurements simulated here continuously sample certain quasi-stationary eddies, for example, the heterogeneity-induced organized motion. Our analysis illustrates how heterogeneity can bias point measurements of vertical flux, and hence their interpretation, in the free-convective PBL.

7. Summary and conclusions

Investigations of the PBL response to land surface heterogeneity are presented from large-eddy simulations coupled with a fully interactive land surface model. Initial temperature and moisture conditions taken from SGP97 measurements are specified as initial soil conditions. Idealized initial PBL profiles are chosen with the intention to evaluate the influence of atmospheric demand for moisture on the coupled response. No mean wind is imposed and a specified incoming solar radiation of 700 W m^{-2} is the only external forcing in the simulations. All simulations reached a quasi-steady state during our analysis time period.

Instantaneous slices of the PBL show dramatic modification of the PBL structure resulting from soil moisture heterogeneity. Consistent with previous research, under free convective conditions, heterogeneity generates stationary organized motions. Because of the atmosphere–land surface couplings we find that the strongest (optimal) PBL response to soil-moisture heterogeneity occurs at scales ranging from $\lambda/z_i \sim 4$ to 9. This scale selectivity is a consequence of the interaction between the organized motions and the induced surface fluxes. Over the optimum scale range, rising motion over the dry side of the heterogeneity is confined to a narrow region and is stronger in magnitude compared to the sinking motion over the wet side. In other words, the patch-induced vertical velocity field is skewed. The $\lambda/z_i \sim 4$ to 9 cases induce the greatest PBL response as the pressure gradients generated by the heterogeneity is largest compared to the other cases. Heterogeneity

makes the buoyantly forced PBLs appear more like combined shear-buoyancy PBLs due to the induced organized circulations.

The organized motions induced at these scales of heterogeneity increase the bulk turbulence kinetic energy of the PBL by about 20% but have little effect on the entrainment rate. With surface heterogeneity, the entrainment rate is not proportional to the total amount of TKE.

The importance of the organized motions differs for dynamical and scalar fields and depends on the scale of the heterogeneity λ, the boundary layer height z_i, and the initial moisture state of the PBL. For cases with $4 < \lambda/z_i < 9$, the patch-induced motions account for almost all of the vertical mixing ratio flux, while small-scale heterogeneity ($\lambda/z_i < 3$) tends to eliminate the ability of the patch-induced motions to transport water vapor.

Fixed-point measurements of vertical scalar flux (i.e., made from a tower) are prone to sampling error if the measurement takes place over a region of heterogeneity and the mean wind is negligible. The magnitude and direction of the error depends on the location of the measurement with respect to the underlying land surface heterogeneity and on the quantity in question. For example, under free convective conditions a time-averaged point measurement at $x/\lambda = 0.25$ and $z/z_i = 0.1$ would overestimate the vertical water vapor mixing ratio flux by about 3%, while the same measurement at $x/\lambda = 0.75$ would underestimate the flux by about 60%.

Acknowledgments. This work was supported in part by the NASA Land Surface Hydrology program through Contract NAG5-8839. We thank Michael Ek from NCEP for supplying us with the NOAH land surface model and for helpful discussions, and Don Lenschow and Peggy Lemone for comments on an earlier version of this manuscript. We also appreciate suggestions from three anonymous reviewers.

APPENDIX

Numerics

For all variables the LES uses pseudospectral differencing in the horizontal. For velocities the LES uses second-order centered-in-space differencing, while for scalars the monotone advection scheme of Koren (1993) is used. Spalart et al.'s (1991) third-order Runge–Kutta scheme advances all fields in time using a fixed Courant–Friedrichs–Lewy number of 0.63 for a complete 3-stage time step. Periodic boundary conditions are imposed in the horizontal. To allow the propagation of gravity waves out of the top of the domain, the upper boundary condition is that of Klemp and Durran (1983). Because the LES uses spectral differencing in the horizontal, the Message Passing Interface (MPI) implementation breaks up the domain in the vertical into slabs of horizontal data residing on a single processor. To perform the spectral decomposition, we use NCAR's FFTPACK version 4.1 (http://www.scd.ucar.edu/softlib/FFTPACK.html).

Details regarding the surface energy balance: R_n is the net radiation, which can be broken down into the sum of its parts: $R_n = R_s(1 - \alpha) + \epsilon R_{\mathrm{dn}} - \epsilon\sigma T_s^4$, where R_s is the incoming solar radiation, α is the albedo of the surface, ϵ is the surface emissivity, R_{dn} is the downwelling longwave radiation, σ is the Stefan–Boltzman constant, and T_s is the surface temperature. Also, H is the sensible heat flux, parameterized as $-\rho c_p C_h U(\theta_a - \theta_s)$ where ρ is the air density, c_p is the specific heat of the air, C_h is an exchange coefficient for heat, U is the wind speed immediately above the surface, and θ_a and θ_s are the potential temperature of the air and ground surface, respectively; LE is the latent heat flux, parameterized as $-\rho L C_e U(q_a - q_s)$, where L is the latent heat of vaporization; C_e is an exchange coefficient for vapor; and q_a and q_s are water vapor mixing ratio of the air and ground surface, respectively; G is the soil heat flux which can be parameterized as

$$k_T(\Theta_1)\frac{T_s - T_1}{z_1},$$

where $k_T(\Theta_1)$ is the soil thermal conductivity that depends on the soil moisture Θ_1 at the first soil level z_1 and soil type. There are potentially other terms in the SEB such as contributions from precipitation, melting snow, horizontal advection, or storage, which we ignore. Mechanistically, the atmosphere is also coupled to land surface through the surface momentum flux. The surface momentum flux is parameterized as $\tau = \rho u_*^2 = \rho C_m U^2$, where u_* is the friction velocity and C_m is the drag coefficient. Through dynamic calculation of τ, R_n, H, LE, and G the atmosphere is therefore directly coupled to the land surface.

In the LSM, upwind finite differences are used for vertical derivatives and the Crank–Nicholson scheme is used for time differencing. At the lower boundary of the LSM, the hydraulic diffusivity is assumed to be zero so that the soil water flux is determined solely by gravitational conduction and the soil heat flux is computed from a vertical temperature gradient between the lowest LSM model level and a specified soil temperature at an imaginary grid point one meter below the bottom of the model. Further details can be found in Mahrt and Pan (1984), Pan and Mahrt (1987), and Chang et al. (1999). To improve scalability when solving the LSM for the coupled surface boundary condition, we use MPI to break up the calculation in the x direction.

REFERENCES

Albertson, J. D., and M. B. Parlange, 1999: Natural integration of scalar fluxes from complex terrain. *Adv. Water Resour.,* **23,** 239–252.

——, W. P. Kustas, and T. M. Scanlon, 2001: Large-eddy simulation over heterogeneous terrain with remotely sensed land surface conditions. *Water Resour. Res.,* **37,** 1939–1953.

Avissar, R., and T. Schmidt, 1998: An evaluation of the scale at which ground-surface heat flux patchiness affects the convec-

tive boundary layer using large-eddy simulations. *J. Atmos. Sci.,* **55,** 2666–2689.
Baldocchi, D. D., B. B. Hicks, and T. P. Meyers, 1988: Measuring biosphere–atmosphere exchanges of biologically related gases with micrometeorological methods. *Ecology,* **69,** 1331–1340.
Banta, R. M., and A. B. White, 2003: Mixing-height differences between land use types: Dependence on wind speed. *J. Geophys. Res.,* **108,** 4321, doi:10.1029/2002JD002748.
Berger, B. W., K. J. Davis, C. Yi, P. S. Bakwin, and C. Zhao, 2001: Long-term carbon dioxide fluxes from a very tall tower in a northern forest. Part I: Flux measurement methodology. *J. Atmos. Oceanic Technol.,* **18,** 529–542.
Brutsaert, W., 1982: *Evaporation into the Atmosphere.* Kluwer Academic, 299 pp.
Chang, S., D. Hahn, C.-H. Yang, and D. Norquist, 1999: Validation of the CAPS model land surface scheme using the 1987 Cabauw/PILPS dataset. *J. Appl. Meteor.,* **38,** 405–422.
Davis, K. J., N. Gamage, C. R. Hagelberg, C. Kiemle, D. H. Lenschow, and P. P. Sullivan, 2000: An objective method for deriving atmospheric structure from airborne LIDAR observations. *J. Atmos. Oceanic Technol.,* **17,** 1455–1468.
Deardorff, J. W., 1979: Prediction of convective mixed-layer entrainment for realistic capping inversion structure. *J. Atmos. Sci.,* **36,** 424–436.
Dyer, A. J., 1981: Flow distortion by supporting structures. *Bound.-Layer Meteor.,* **20,** 243–251.
Esau, I. N., and T. J. Lyons, 2002: Effect of sharp vegetation boundary on the convective atmospheric boundary layer. *Agric. For. Meteor.,* **114,** 3–13.
Finnigan, J. J., R. Clement, Y. Malhi, R. Leuning, and H. Cleugh, 2003: A re-evaluation of long-term flux measurement techniques. Part I: Averaging and coordinate rotation. *Bound.-Layer Meteor.,* **107,** 1–48.
Garratt, J. R., 1993: Sensitivity of climate simulations to land-surface and atmospheric boundary-layer treatments—A review. *J. Climate,* **6,** 419–448.
Hadfield, M. G., W. R. Cotton, and R. A. Pielke, 1991: Large-eddy simulations of thermally forced circulation in the convective boundary layer. Part I: A small scale circulation with zero wind. *Bound.-Layer Meteor.,* **57,** 79–114.
Hechtel, L. M., C.-H. Moeng, and R. B. Stull, 1990: The effects of nonhomogeneous surface fluxes on the convective boundary layer: A case study using large-eddy simulation. *J. Atmos. Sci.,* **47,** 1721–1741.
Hussain, A. K. M. F., and W. C. Reynolds, 1970: The mechanics of an organized wave in turbulent shear flows. *J. Fluid Mech.,* **41,** 241–258.
Jackson, T. J., cited 1997: Southern Great Plains 1997 (SGP97) Hydrology Experiment Plan. [Available online at http://hydrolab.arsusda.gov/sgp97/.]
Kaimal, J. C., and J. J. Finnigan, 1994: *Atmospheric Boundary Layer Flows: Their Structure and Measurement.* Oxford University Press, 289 pp.
Kanda, M., A. Inagaki, M. O. Letzel, S. Raasch, and T. Watanabe, 2004: LES study of the energy imbalance problem with eddy covariance fluxes. *Bound.-Layer Meteor.,* **110,** 381–404.
Klemp, J. B., and D. R. Durran, 1983: An upper boundary condition permitting internal gravity wave radiation in numerical mesoscale models. *Mon. Wea. Rev.,* **111,** 430–444.
Koren, B., 1993: A robust upwind discretization method for advection, diffusion and source terms. *Numerical Methods for Advection–Diffusion Problems,* C. B. Vrengdenhil and B. Koren, Eds., Notes on Numerical Fluid Mechanics, Vol. 45, Vieweg Verlag, 117–138.
Kustas, W. P., and J. D. Albertson, 2003: Effects of surface temperature contrast on land–atmosphere exchange: A case study from Monsoon 90. *Water Resour. Res.,* **39,** 1159, doi:10.1029/2001WR001226.
Letzel, M. O., and S. Raasch, 2003: Large eddy simulation of thermally induced oscillations in the convective boundary layer. *J. Atmos. Sci.,* **60,** 2328–2341.
Lilly, D. K., 2002: Entrainment into mixed layers. Part I: Sharp-edged and smoothed tops. *J. Atmos. Sci.,* **59,** 3340–3352.
Mahrt, L., 1998: Flux sampling errors for aircraft and towers. *J. Atmos. Oceanic Technol.,* **15,** 416–429.
——, and H. Pan, 1984: A two-layer model of soil hydrology. *Bound.-Layer Meteor.,* **29,** 1–20.
——, D. Vickers, and J. Sun, 2001: Spatial variations of surface moisture flux from aircraft data. *Adv. Water Resour.,* **24,** 1133–1141.
McNaughton, K. G., and M. R. Raupach, 1996: Responses of the convective boundary layer and the surface energy balance to large-scale heterogeneity. *Scaling up in Hydrology Using Remote Sensing,* J. B. Stewart et al., Eds., John Wiley & Sons, 171–182.
Moeng, C.-H., and P. P. Sullivan, 1994: A comparison of shear- and buoyancy-driven planetary boundary layer flows. *J. Atmos. Sci.,* **51,** 999–1022.
Pan, H.-L., and L. Mahrt, 1987: Interaction between soil hydrology and boundary layer development. *Bound.-Layer Meteor.,* **38,** 185–202.
Patton, E. G., P. P. Sullivan, and C.-H. Moeng, 2004: The influence of idealized heterogeneity on convective planetary boundary layers coupled to the land surface. National Center for Atmospheric Research Tech. Note NCAR/TN-462+STR, 71 pp. [Available online at http://www.library.ucar.edu/uhtbin/hyperion-image/DR000662.]
Paulson, C. A., 1970: The mathematical representation of wind speed and temperature profiles in the unstable atmospheric surface layer. *J. Appl. Meteor.,* **9,** 857–861.
Raasch, S., and G. Harbusch, 2001: An analysis of secondary circulations and their effects caused by small-scale surface heterogeneities using large-eddy simulation. *Bound.-Layer Meteor.,* **101,** 31–59.
Raupach, M. R., 2000: Equilibrium evaporation and the convective boundary layer. *Bound.-Layer Meteor.,* **96,** 107–141.
Rowntree, P. R., and J. Bolton, 1983: Simulation of the atmospheric response to soil moisture anomalies over Europe. *Quart. J. Roy. Meteor. Soc.,* **109,** 501–526.
Roy, S. B., and R. Avissar, 2000: Scales of response of the convective boundary layer to land-surface heterogeneity. *Geophys. Res. Lett.,* **27,** 533–536.
Segal, M., and R. W. Arritt, 1992: Nonclassical mesoscale circulations caused by surface sensible heat-flux gradients. *Bull. Amer. Meteor. Soc.,* **73,** 1593–1604.
Seth, A., and F. Giorgi, 1996: Three-dimensional model study of organized mesoscale circulations induced by vegetation. *J. Geophys. Res.,* **101**, 7371–7391.
Shen, S., and M. Y. Leclerc, 1995: How large must surface inhomogeneities be before they influence the convective boundary layer structure? A case study. *Quart. J. Roy. Meteor. Soc.,* **121,** 1209–1228.
Spalart, P. R., R. D. Moser, and M. M. Rogers, 1991: Spectral methods for the Navier–Stokes equations with one infinite and two periodic directions. *J. Comput. Phys.,* **96,** 297–324.
Sullivan, P. P., J. C. McWilliams, and C.-H. Moeng, 1996: A grid nesting method for large-eddy simulation of planetary boundary-layer flows. *Bound.-Layer Meteor.,* **80,** 167–202.
——, ——, and ——, 2000: Simulation of turbulent flow over idealized water waves. *J. Fluid Mech.,* **404,** 47–85.
——, C.-H. Moeng, B. Stevens, D. H. Lenschow, and S. D. Mayor, 1998: Structure of the entrainment zone capping the convective atmospheric boundary layer. *J. Atmos. Sci.,* **55,** 3042–3064.
Weaver, C. P., and R. Avissar, 2001: Atmospheric disturbances caused by human modification of the landscape. *Bull. Amer. Meteor. Soc.,* **82,** 269–281.
Zeng, X., and R. A. Pielke, 1995: Landscape-induced atmospheric flow and its parameterization in large-scale numerical models. *J. Climate,* **8,** 1156–1177.